A Microfluidic, Extensional Flow Device for Manipulating Soft Particles

by

Ali Hussain Motagamwala

A thesis submitted in conformity with the requirements for the degree of
Masters of Applied Science

Department of Chemical Engineering and Applied Chemistry
University of Toronto

A Microfluidic, Extensional Flow Device for Manipulating Soft Particles

Ali Hussain Motagamwala

Masters in Applied Science

Department of Chemical Engineering and Applied Chemistry
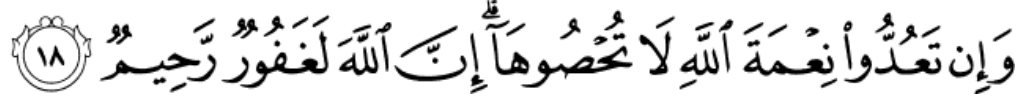University of Toronto

2013

Abstract

A computer-controlled microfluidic extensional flow device is developed for trapping and manipulating micron-sized hard and soft particles. The extensional flow is generated in a diamond-shaped cross-slot that has each corner connected to a pressure-controlled liquid reservoir. By employing an imaging-based control algorithm, a particle can be made to move to an arbitrary position within the slot by adjusting the reservoir pressures and hence the fluid flow rates into/out of the slot. Thus, a soft particle can be trapped indefinitely at a point within the slot, and a known hydrodynamic force can be applied to study the dynamics of stretching and breakup of the particle. Alternatively, adhesion or coalescence dynamics of soft particles may be investigated by effecting a controlled collision between two particles. The device is validated by measuring the low interfacial tension of a compatibilized oil-water interface.

»

Acknowledgments

وَإِن تَعُدُّواْ نِعْمَةَ ٱللَّهِ لَا تُحْصُوهَآ إِنَّ ٱللَّهَ لَغَفُورٌ رَّحِيمٌ ۝

Table of Contents

Contents

List of Tables

List of Figures

List of Appendices

Chapter 1

1   Introduction

We report the development of a computer-controlled, microfluidic extensional flow device to trap and manipulate a single, soft particle in a flowing fluid. By soft, we imply that the particle deforms from its equilibrium shape under the natural forcing conditions that exist in the mixture of the particle and the fluid. For example, consider an emulsion, i.e., a mixture of drops of one fluid suspended in another immiscible fluid, being transported in a tube. At sufficiently high flow rates through the tube, the shape of the drop departs from its equilibrium spherical shape, and the drop may even break up into smaller droplets.

Mixtures of soft particles and liquids, or soft particle suspensions, are ubiquitous, and we encounter them on daily basis in various forms: lotions, creams, fabric softeners, tonics, adhesives, liquid detergents, mayonnaise, ice-cream, etc. Such mixtures are prevalent in petroleum extraction [1], food manufacture, wastewater treatment plants, the grain/oilseed milling industry, the detergents/fabric enhancer industry [2], pharmaceutical industry [3], and polymer blending [4]. These dispersions also exist within our bodies. For example, blood is a mixture of plasma and three major types of soft particles: red blood cells, white blood cells and platelets. Thus, soft particle suspensions represent an extremely important class of materials.

Unfortunately, dispersions containing soft particles are ordinarily extremely difficult to understand and characterize at the multi-particle, concentrated level. This is because the formulation procedures for such mixtures are mostly developed empirically, and the basic relationships that connect the macroscopic properties of the mixture to its microscopic properties are often missing. If these relationships are understood, we could have better material properties (e.g. product function, product stability), and minimize environmental impact in the manufacturing process.

To unearth structure-property relationships for soft particle suspensions, a promising method is the bottom-up approach, whereby the material behavior is understood at the level of a single or

few particles. By understanding the interaction behaviors for a small number of particles, some general trends in more concentrated systems can be predicted. As an example, the efficiency of separation of the droplets of oil in an oil-in-water emulsion by gravity or centrifugation increases with an increasing diameter of the oil droplets. Hence, coalescence between two droplets, which increases the average size of the droplets, is beneficial for separation, while drop break-up, which reduces drop size, slows down separation. Such considerations become more important when surfactants are used to decrease the interfacial tension in such processes as enhanced oil recovery [5], which may lead to the formation of stable emulsions. Thus, to design an efficient process for oil-water separation, it is vital to know not only the kinetics, but also the mechanisms of coalescence and breakup of oil drops.

The primary motivation behind designing the extensional flow device in this work is to establish a platform where the breakup of a single soft particle, and aggregation/fusion of a pair of soft particles, may be investigated systematically. To study break-up, the device provides the facility to trap a soft particle in a region where the stretching rate is fairly constant, and to maintain it there to visualize the stretching and breakup of the particle. Alternatively, two soft particles can be swept into the region of a constant compressional rate, and can be monitored for adhesion or fusion. But before we discuss the details of our device, we discuss past attempts at building such a device, and how our device is superior to these.

1.1   Literature review

The ability to precisely control a particle/drop position in an extensional flow is a very powerful tool to study a wide range of phenomena. Hence, much attention has been paid in the last two decades to develop a diverse set of tools to achieve control over particle position and velocity in a flowing fluid. The most common techniques employ either magnetic [6] [7] [8], optic [9] [10] acoustic [11] [12] [13] or hydrodynamic [14] [15] [16] [17] [18] force fields to confine and/or manipulate particles.

In the optical force field method, a tightly focused laser beam traps and manipulates particles with very high precision. The power of the laser required for trapping increases with a decrease in the particle size, which leads to an increase in the local temperature of the suspending

medium. Another disadvantage is that for soft particles such as vesicles, the laser beam can actually influence the particle structure, which is undesirable in characterization studies. The size of the particle that can be trapped using optical tweezers ranges from a few Angstroms up to a micrometer [19] and the maximum force that can be applied is in the range of a couple of hundred picoNewton (pN) [20]. Though this order of forces is great to study the dynamics of single molecules like DNA, it cannot be used to study the dynamics of drops or vesicles. Similarly, only magnetically-active particles can be trapped and manipulated with magnetic force fields and acoustic trapping requires a high frequency sound wave to create a pressure node where particles are trapped. Hydrodynamic force fields do not pose such problems, and thus can be used to trap/manipulate particles of any size and kind, of particles as long as the particle position can be accurately determined [21].

Particle trapping using hydrodynamic forces is not, however, a new concept. In 1934, G. I. Taylor developed a four-roll mill apparatus to generate mixed flows that can be varied from purely rotational to shear to purely extensional by varying the speed and direction of rotation of four cylindrical rollers. Taylor used the four-roll mill to study drop deformation in an irrotational flow by bringing a single drop of oil at the stagnation point of the flow [14]. But, since the stagnation point position is not a stable equilibrium position for a drop, in any linear flow other than a purely extensional flow, a continuous control of the drop position is required for restricting the position of the drop. Thus, the study of drop dynamics in these flows with strong extensional components was limited by the inability to quickly change the flow field in order to trap the drop.

Pioneering work by the Leal group lead to the development of a computer-controlled four-roll mill. The ability to control the drop position with a computer enabled them to trap a drop at the stagnation point of the linear flow for extended periods of time. The computer control also enabled the study of drop dynamics for mixed flows that were not possible with manual control. Thus, the study of the deformation of viscous drops which requires a long time was performed, and improved data was obtained for a wide range of viscosity ratio (10^{-3} to 10^{2}) [15]. Apart from single drop deformation studies, the computer-controlled four-roll mill was also used to study the coalescence of viscous droplets. Both head-on [22] and glancing [23] collisions were studied at various capillary numbers and the critical capillary number versus drop size was determined. However, the fabrication of the four-roll mill is involved and expensive. Also, the large size of

the device (10 cm x 10 cm x 10 cm) imposes strong restrictions on the densities of the fluids, the viscosities of the fluids, and the sizes of the drops that may be employed in the experiments, to avoid settling effects.

One of the first attempts to make a four roll mill on a microfluidic platform was undertaken by Hudson and co-workers [24]. Their microfluidic four roll mill consisted of six intersecting channels with baffles between channels in a chiral arrangement. A microfluidic four roll mill with symmetric channels was developed by Lee et al. [17]. They were able to produce all types of flows by appropriately choosing the flow rates in each channel. With both these devices, symmetric as well as asymmetric, it was easy to produce purely extensional and simple shear flows, but it was difficult to generate strong rotational flows [17]. These devices were controlled manually, and therefore, particle trapping at the stagnation point for long times were not achievable. Also, with manual control, it was impossible to manipulate a particle along a predefined path.

More recent attempts at single particle trapping and controlled steering in a microfluidic device have employed active feedback control of the stagnation point position. Shapiro and coworkers [25] [18] and Cohen et al. [26] [27] [28], have developed a feedback control mechanism with a corrective electrokinetic flow, that induces a drift to direct the particle to a desired position. Using this method, Shapiro and coworkers controlled a single fluorescent nanocrystal in a viscous solution to a remarkable precision of ~50 nm. Cohen et. al., used the Anti-Brownian Electrokinetic (ABEL) trap to restrict a fluorescent polystyrene bead to a precision of 140 nm. The electrokinetic trap is capable of isolating a single particle, but could be prone to diffusion of other particles into the trapping area. Although electrokinetic flows are easy to implement and more precisely controlled, they are highly dependent on the surface properties of the channel. It is important, therefore, that solutes that are capable of being adsorbed on the channel surface and modifying its properties are absent from the suspending fluid, since this can interfere strongly with any control algorithm used to alter the flow rate in the microchannel. Also, the presence of ions in the suspending fluid to create the counterion-cloud is essential for electrosmotic flows. This restricts the applicability of the electrokinetic trap, e.g. it cannot be used to study the dynamics of water drops in oil.

Recently, Schroeder et. al. have constructed a cross-slot device that employs hydrodynamic forces to trap and manipulate a single particles, and in particular, polymer molecules [16] [29]. This device (shown in Fig 1.1) has two inlets and two outlets, and produces a pure extensional flow at the center of the slot. In this pressure-driven hydrodynamic trap, the hydrodynamic resistance of one inlets and one outlet is adjusted by using a pneumatic, Polydimethylsiloxane (PDMS)-based valve, thereby altering the flow rate through the inlet and outlet and in turn the stagnation point position. However, their group has not yet tried to apply their device to study soft particles.
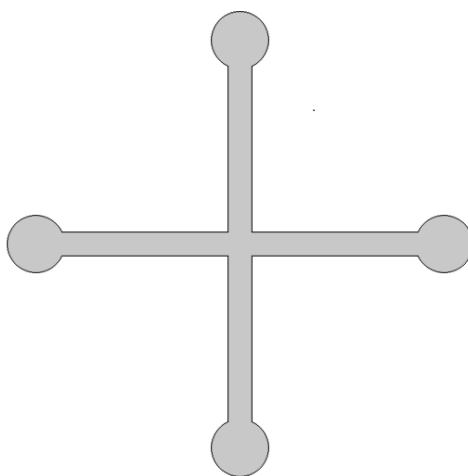
Figure 1.1 Schematic of cross-slot device employed by Schroeder et. al. [29].

In this work, we design an extensional flow device with a new geometry, and adapt it for performing experiments with soft particles. Unlike previous designs, we employ a flow geometry that permits an analytical solution of the flow field, which can be integrated with the control process. The proposed new design has a higher region of constant strain rate as compared to the square cross-slot design. We demonstrate the use of the microfluidic extensional flow device to evaluate low to ultralow interfacial tensions in emulsion systems. Apart from the spinning drop tensiometer [30], constrained sessile drop method [31] and the recent method using magnetic particles and field [31], this device is perhaps the only other available method for ultralow interfacial tensiometry.

This thesis is organized as follows. Chapter 2 explains the design of the device, its fabrication, the working principle and the materials and methods. Chapter 3 outlines the calibration of

stagnation point position and shear rate, and discusses the algorithm for particle trapping and manipulation. The theoretical framework for determining the interfacial tension with the extensional flow device and the corresponding experiments are discussed in chapter 4. Chapter 5 suggests a number of improvements to the device, and some soft particle analyses that can be implemented with it in the future.

Chapter 2

2   Operating Principle, Experimental Methods and Materials

2.1   Geometry of the microfluidic extensional flow device

Fig. 2.1 shows the schematic of the microfluidic extensional flow device used in this study. It is a diamond-shaped cross-slot that has each corner connected to a liquid reservoir. The liquid reservoir is pressurized, and the pressure difference between the reservoirs causes the flow through the device. The flow rate through the inlets (I_1, I_2) and the outlets (O_1, O_2) and, in turn, the stagnation point position in the slot can be changed by altering the pressures maintained in the reservoirs.
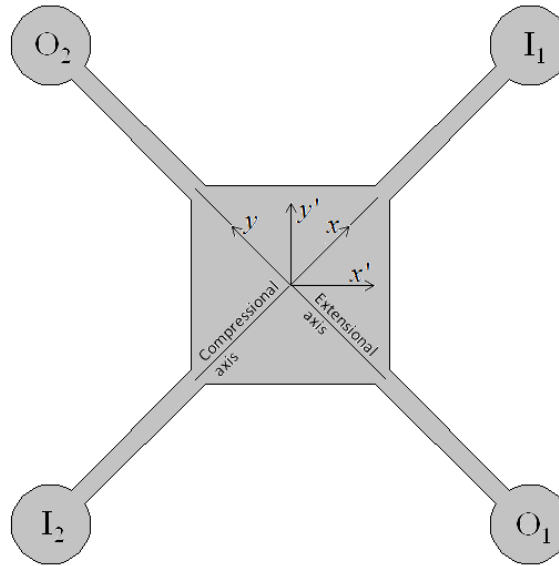
Figure 2.1. Schematic of the microfluidic extensional flow device used in this study. In the diagram, I_1, I_2 and O_1, O_2 represent the inlets and outlets of the device respectively. Line joining I_1 and I_2 is the compressional axis and the line joining O_1 and O_2 is the extensional axis. (x,y) is the coordinate system with respect to the compressional and extensional axes. (x',y') represents the horizontal and vertical coordinate system.

The flow field for equal flow through the inlets and outlets is shown in Fig. 2.2. The strain rate in the device is defined as, $G = \sqrt{\frac{1}{2}(\gamma : \gamma)}$ where, $\gamma = \nabla \mathbf{u} + (\nabla \mathbf{u})^T$. Contour plots of the strain rates in the two geometries are shown in Fig. 2.3. The contours level curves show the strain rate in s^{-1}. The levels are chosen such that the successive levels are in 2% increment/decrement in strain rates. The soft particle stretching and collision experiments are performed at the center, because this is in the region where the variation in strain rate is minimum.

An advantage of our design over the conventional square cross slot design is that for the same device depth, strain rate at the center and fluid flow rate, our design has a higher area of constant strain rate. For the diamond geometry, when the stagnation point is at the device center, the strain rate at the center can be written as,

$$G_d = k_d \frac{Q_d}{W_d^2}. \tag{2.1}$$

The area over which the variation of the strain rate is only 2% from the value at the center is

$$A_d = f_d W_d^2. \tag{2.2}$$

Here, f_d is the fraction of the diamond slot for which the variation in the strain rate is less than 2% from that of the center. For the square cross-slot geometry, we have, similarly,

$$G_s = k_s \frac{Q_s}{W_s^2}, \tag{2.3}$$

$$\text{and, } A_s = f_s W_s^2. \tag{2.4}$$

We calculate this area by finding the largest circle in which the strain rate varies by only 2%. The region where the strain rate is within 2% is shown in Fig. 2.3(a) and 2.3 (b) for the diamond and cross-slot, respectively. To have the same strain rate at the center in the two geometries at the same flow rate, we must have

$$\left(\frac{W_d}{W_s}\right)^2 = \frac{k_d}{k_s}. \tag{2.5}$$

The ratio of the areas, therefore, is

$$\frac{A_d}{A_s} = \frac{f_d}{f_s}\frac{W_d^2}{W_s^2} = \frac{f_d}{f_s}\frac{k_d}{k_s}. \tag{2.6}$$

For the device depth of 100 μm, center strain rate of 0.691 s^{-1} and flow rate of 26 μl/hr

$$k_d = 0.691\left(\frac{(1000\times10^{-6})^2}{7\times10^{-12}}\right) = 9.87\times10^4 \qquad f_d = \frac{\pi\left(161\times10^{-6}\right)^2}{\left(1000\times10^{-6}\right)^2} = 0.0814$$

$$k_s = 0.691\left(\frac{\left(616\times10^{-6}\right)^2}{7\times10^{-12}}\right) = 37457.7 \qquad f_s = \frac{\pi\left(135\times10^{-6}\right)^2}{\left(616\times10^{-6}\right)^2} = 0.151 \tag{2.7}$$

$$\frac{A_d}{A_s} = 1.42.$$

Thus, the area for which the strain rate near the device center changes by only 2% is 42% larger for the new design as compared to the square cross-slot design.

An important feature of the flow geometry we have selected is that it permits an analytical solution of the flow field (Appendix I), and can, thus, allow the implementation of a model-based control to steer a particle to the stagnation point. For the studies discussed in this thesis, proportional control was found to suffice, but in order to exercise improved control (e.g. to minimize oscillations of the particle near the stagnation point particularly at higher strain rates), a model predictive control based on the analytical solution will be implemented in the future.
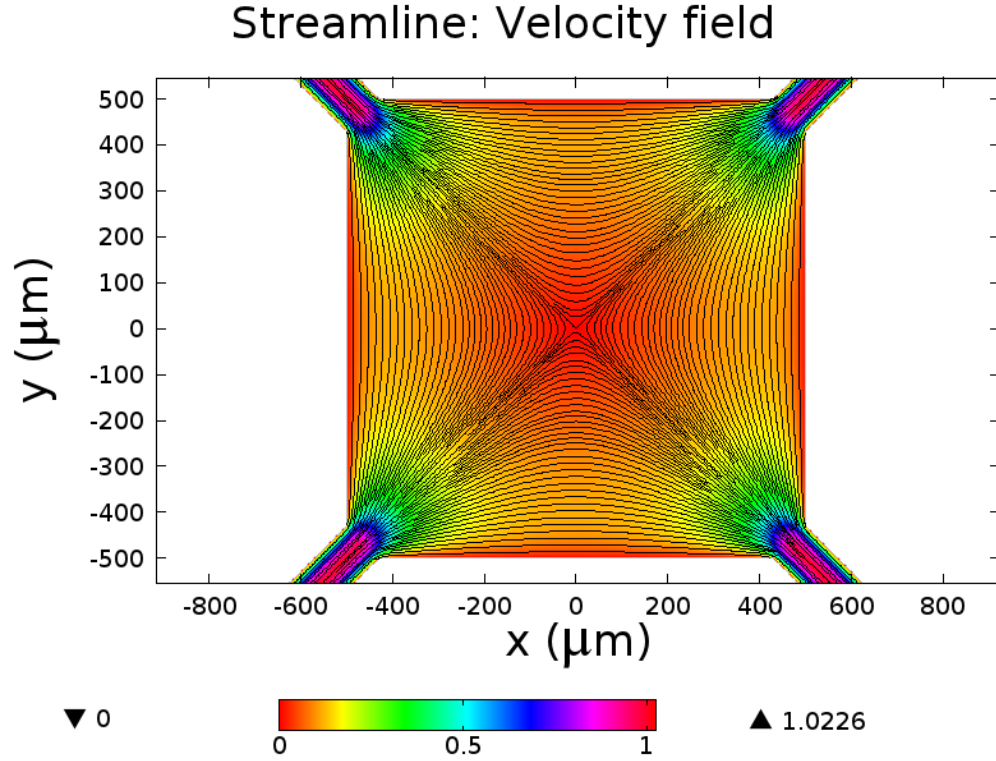
Figure 2.2. A streamline plot of a diamond microfluidic extensional flow device simulated in COMSOL®. Inlet and outlet flow rates are 26 μl/hr. The surface plot represents the velocity in mm/s.

2.2   Working principle

The principal idea behind particle manipulation in the extensional flow device is that the velocity of the particle in the slot can be adjusted by suitably placing the stagnation point of the flow around the particle. For example, consider a particle placed at the center of the device. If the particle is required to be moved towards I_1, I_2, O_1 or O_2, as shown in Fig. 2.4, then the stagnation point needs to be shifted towards I_1, I_2, O_2 and O_1, respectively, in order to produce the necessary velocity in these directions.   Hence, by appropriately positioning the stagnation point, the particle can be made to move along an arbitrary path in the slot.   This strategy is used to bring a soft particle to the device center to perform a stretching experiment. However, once the particle is brought to the center, we have another challenge - maintaining the particle at the center [14, 15].
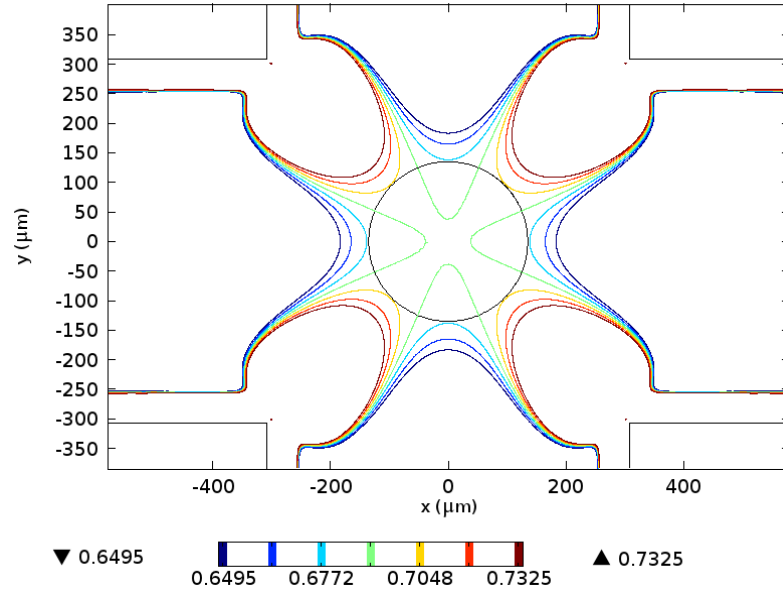
(a)
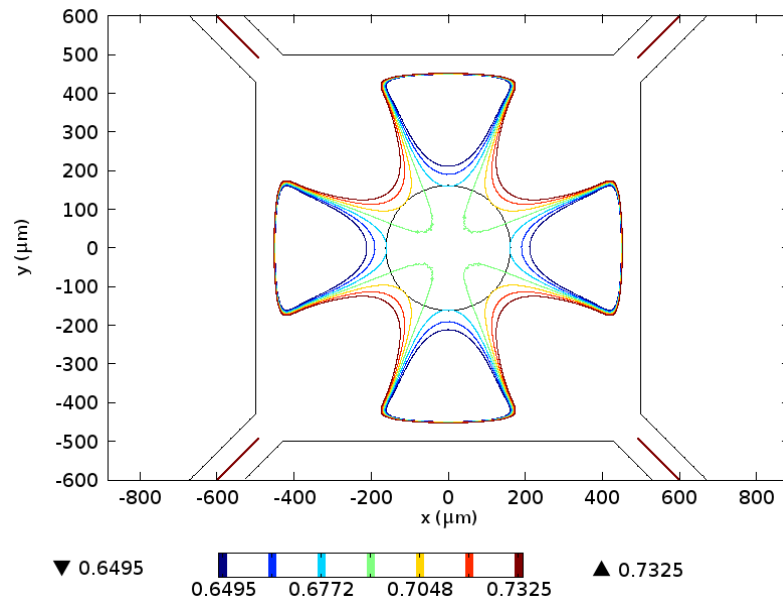
(b)

Figure 2.3. Level curves of the strain rate for the (a) cross-slot used by previous investigators, and (b) our extensional flow geometry. The circle, drawn in black, is the largest circle for which the strain rate varies by 2%.

The flow of an incompressible fluid through the microfluidic device generates a potential flow in which the velocity potential has a saddle point at the stagnation point due to the incompressibility of the fluid. The stagnation point represents a stable force equilibrium along the compressional axis (see fig 2.1), but an unstable one along the extensional axis. In other words, small fluctuations of the particle position along the compressional axis decay, but such fluctuations along the extensional axis grow exponentially in time, and will eventually cause the particle to move away from the stagnation point. An active control is required, therefore, to maintain the particle at this point. Quite conveniently, this also can be achieved by manipulating the stagnation point as discussed in the previous paragraph and the particle can be maintained at the center virtually indefinitely over a certain range of strain rates. This is demonstrated in chapter 3 by controlling a fluorescent particle at the center stagnation point for up to 15 min.

(a)   (b)

(c)   (d)
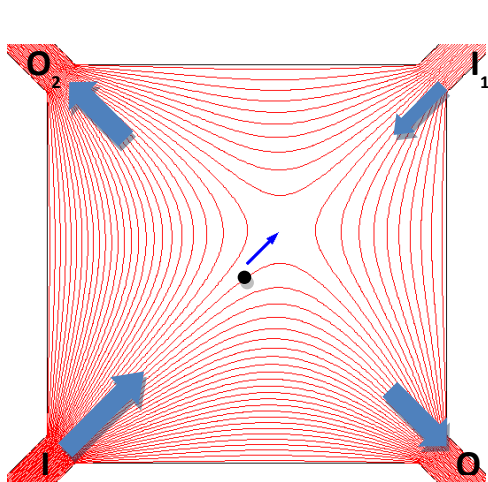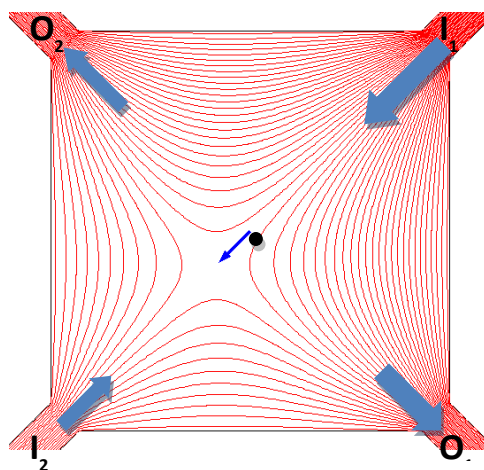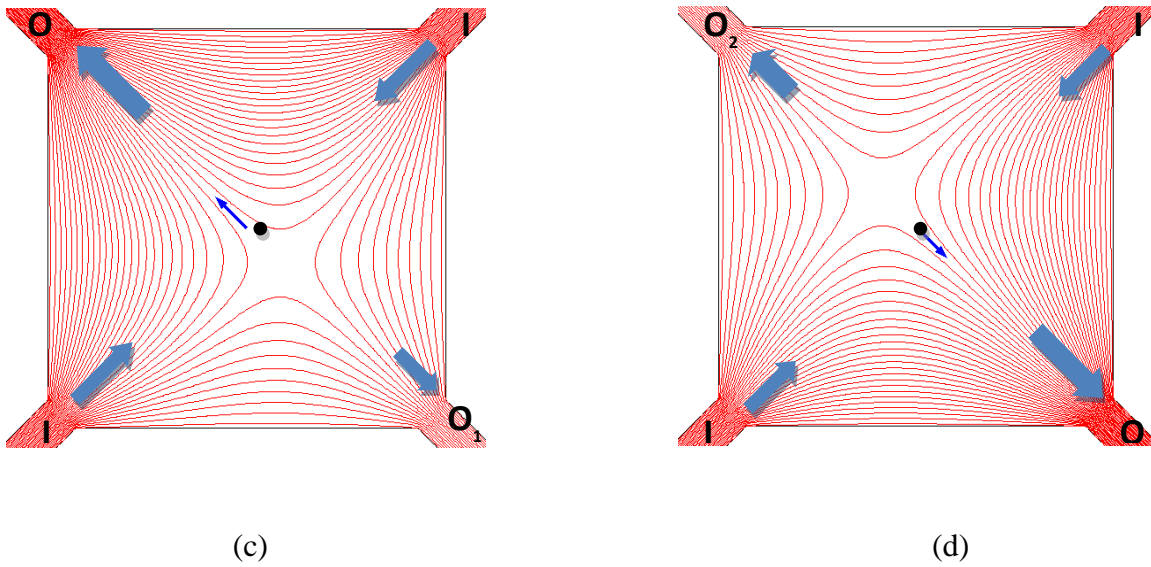
Figure 2.4. Particle steering in any direction. (a) Particle steered towards I_1. (b) Particle steered towards I_2. (c) Particle steered towards O_1. (d) Particle steered towards O_2.   The sizes of the arrows drawn adjacent to the inlets or outlets are directly related to the flow rates in these ports.

2.3   Microfluidic circuit

To adjust the position of the stagnation point, the flow rates of the fluid in the four channels need to be manipulated; this is achieved using four pressure-controlled reservoirs. The schematic of the flow circuit is given in Fig. 2.5. An electrical-to-pneumatic controller is used to change the pressure in the reservoirs. Due to the difference in the pressure between the reservoirs the fluid flows through the tubing and into/out of the device.
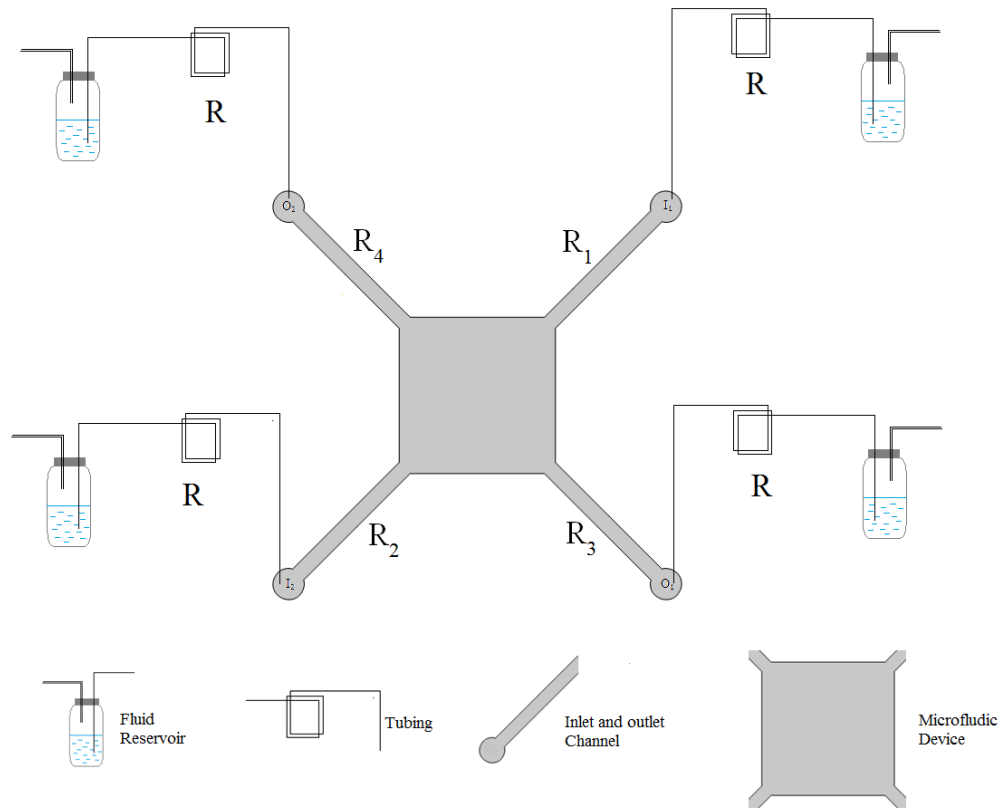
Figure 2.5 Schematic of the flow device and connection to the fluid reservoirs. R_1, R_2, R_3 and R_4 are the hydrodynamic resistances of each arm of the diamond slot and R is the hydrodynamic resistance of the external circular tubing

The small length scales and low flow rates in these geometries imply that the Reynolds numbers are small. Under these conditions, the relationship between the pressure drop, ΔP, and the flow rate, Q, through a given flow geometry is linear.

$$\Delta P = RQ. \tag{2.8}$$

Here, R is the hydrodynamic resistance which is inversely proportional to the fluid viscosity, μ, and depends only on the geometry of the flow conduit. The above equation at low Reynolds numbers is analogous to Ohm's law,

$$\Delta V = R_{\Omega} I, \tag{2.9}$$

where the electrical variables, ΔV, the voltage difference, R_{Ω}, the electrical resistance, and I, the resulting current, are exact analogs of the flow variables, ΔP, R and Q, respectively. The electrical equivalent of the microfluidic circuit employed in this work is shown in Fig. 2.6. The inlets and outlets channels in the microfluidic device have rectangular cross-sections, and the resistance of each channel is denoted by R_i, where i denotes a particular inlet or outlet. Equal length of circular tubing is used for connecting the microfluidic device to the fluid reservoirs, and the resistance of each tubing is R. If the average pressure in the slot is P_0, the flow rate in each arm is

$$Q_i = \frac{P_i - P_0}{R + R_i}. \tag{2.10}$$
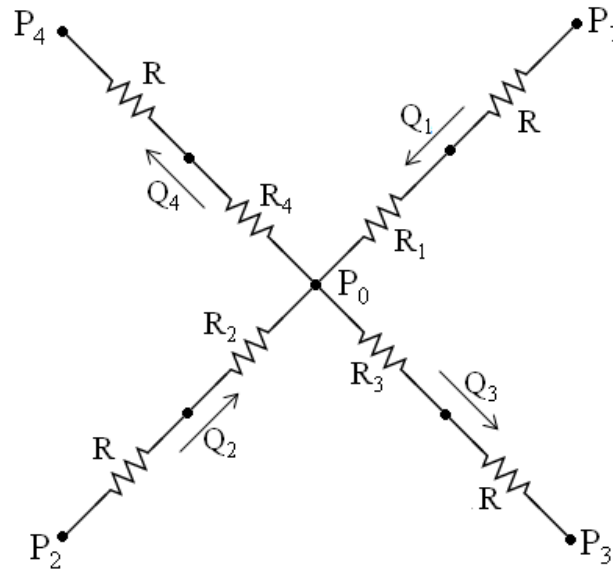
Figure 2.6. Electrical representation of microfluidic channel . P_1, P_2, P_3 and P_4 are the pressure in the reservoirs. Q_1, Q_2, Q_3 and Q_4 are the flow rates through each arm leading to the diamond slot.

The pressure P_0 is obtained by the requirement of incompressibility of the liquid, which imposes

$$\sum_{i=1}^{4} Q_i = 0, \tag{2.11}$$

yielding

$$P_0 = \left(\sum_{i=1}^{4} \frac{P_i}{R+R_i} \right) \bigg/ \left(\sum_{i=1}^{4} \frac{1}{R+R_i} \right). \tag{2.12}$$

The length of the tubing is chosen so that the tubing resistances are much higher than the channel resistances, typically by an order of magnitude. The reason for this choice is as follows. The control algorithm that manipulates particles in the slot is based on flowing fluid at a constant flow rate in each arm of the microfluidic device. When particles flow through an arm, R_i can be modified, which, in turn, could alter the flow rate, Q_i, in the arm. This can interfere with the implementation of the control algorithm. However, if R is chosen such that $R \gg R_i$, the flow rate in each arm is

$$Q_i = \frac{1}{R} \left(P_i - \frac{1}{4} \sum_{i=1}^{4} P_i \right). \tag{2.13}$$

Thus, Q_i becomes independent of the individual resistances, R_i, within the microfluidic device and depends only on the control variables, P_i. Another advantage of maintaining $R \gg R_i$ is that it suppresses the effect of fabrication-induced differences in the resistances of the inlet and outlet arms on the control process.

2.4 Device fabrication

The microfluidic extensional flow device is fabricated in PDMS using the method of soft lithography. This method has been extensively reviewed in the literature [32].

The microfluidic channel was designed using AutoCAD, a computer-aided design and drafting software. The design was then printed at a high resolution of 20,000 DPI on a transparency mask

by Pacific Arts and Design, Toronto. A 100 μm layer of negative photo-resist (SU-8 50) was spin-coated onto a 3" diameter silicon wafer. The wafer was then pre-baked at 95°C for 15 min. The transparency was used as a photo-mask in contact photolithography using a mask aligner with 16 mJ.cm^{-2}.s^{-1} lamp power. The spin-coated SU-8 50 was exposed to UV light (365 nm) for 35 seconds. The unexposed photo-resist was removed by dissolving in SU8 developer, yielding a silicon wafer with a positive low-relief of photoresist that served as a casting mold for PDMS.

PDMS elastomer was mixed with the pre-cursor in the ratio of 10:1, degassed and poured over the cast. The cast was then cured at 73°C for 4 hours. Cured PDMS was cut and carefully peeled off the master. Access holes were punched using an 18 gauge syringe needle. The device was cleaned by sonicating in isopropyl alcohol for 2 minutes and subsequently dried with nitrogen. The base of the device was made using the same procedure, except that a plain silicon wafer without any low-relief feature was used as a master. Finally, the PDMS block with casted micro-channels was bonded to the base PDMS block by oxygen plasma etching. Fig. 2.7 shows an image of a bonded microfluidic extensional flow device.
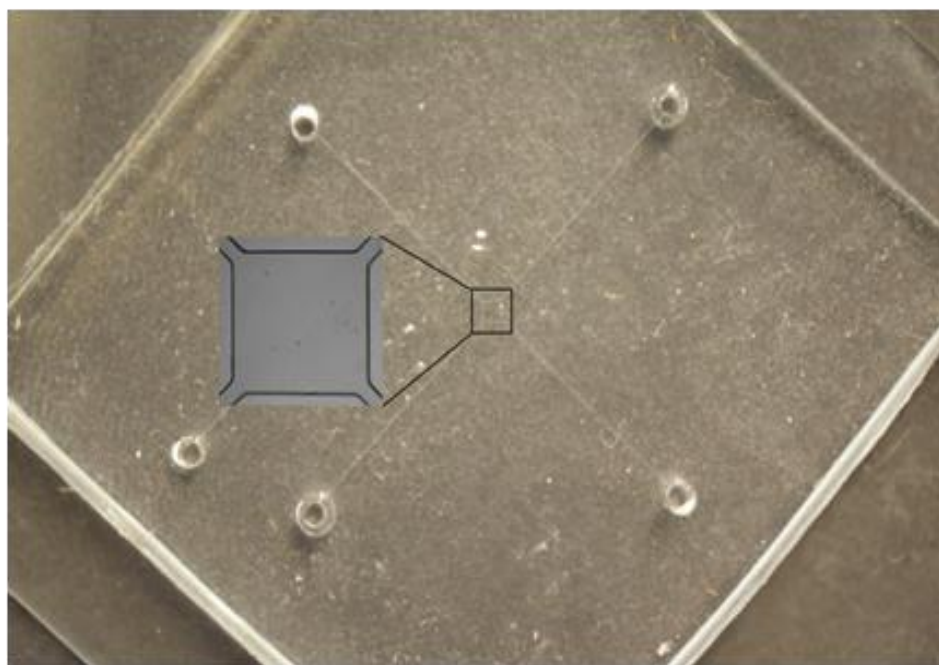
Figure 2.7 Image of the bonded microfluidic extensional flow device. Inset shows the diamond slot for trapping and manipulating particle position.

2.5   Experimental setup

The experimental setup is shown in Fig. 2.8. The extensional flow device was mounted on an inverted microscope (Nikon TI-Eclipse). A 16-bit monochrome camera (Retiga 2000R, Q-imaging) was used as the imaging device. The Image acquisition and Image processing toolboxes of MATLAB$^{®}$ were used to calculate the particle/drop position. The fluid was delivered to the device using rigid PFA tubing (0.01 in. inner diameter 0.0625 in outer diameter). One end of the tubing was inserted into the inlet/outlet of the device and the other end was submerged under the liquid surface in the reservoir. Four 100 ml, GL-45 screw cap glass bottles (Fisherbrand) were used as liquid reservoirs. HPLC caps (IDEX-Health & Science) with three access holes were employed to shut these reservoirs. Since only two access holes were required, one for the PFA tubing, and the other for pressurizing the bottle contents, the third one was blocked using epoxy glue.

The reservoirs are pressurized using Type 2000 pressure transducer (Marsh Bellofram) which regulates an incoming supply pressure down to a precise output that is directly proportional to an electrical control signal. The electrical input to the pressure controller based on a proportional control algorithm is provided through NI-USB 6351 DAQ card.
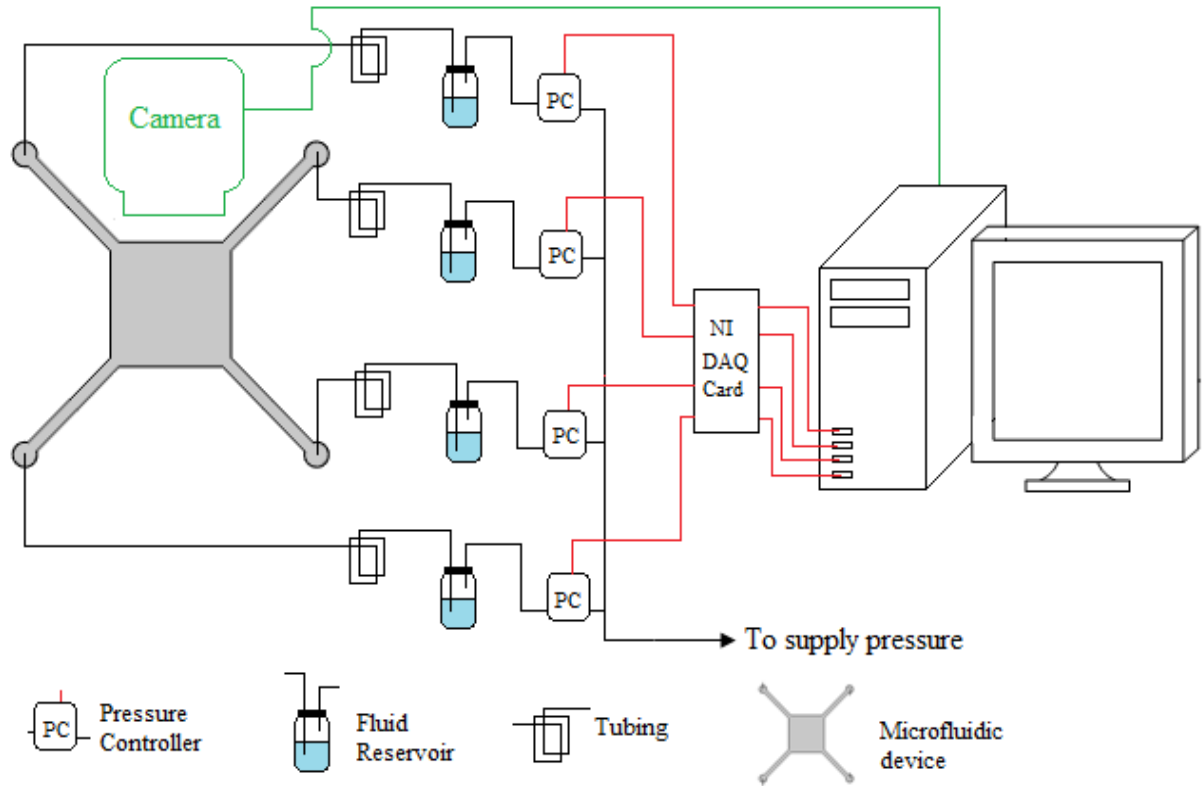
Figure 2.8. Schematic of the complete experimental setup.

2.6 Control scheme

To achieve the control of the particle position at the center stagnation point, we employed a proportional control strategy. The events in one control loop were as follows.

Step 1. The image of the diamond slot (fig. 2.1) of the device was captured using the camera, and read into MATLAB®.

Step 2. The image is convolved with a normalized 5x5 laplacian kernel matrix to determine the positions of the particles in the image. The image is also saved for future analysis.

Step 3. The distance of every particle found in step 2 from the device center is calculated. The particle nearest to the device center is then selected to be steered to the device center.

Step 4. Particle coordinates are transformed to a co-ordinate system based on the extensional and compressional axes (with device center as the origin), by using the following equation (see, also, Fig. 2.1).

$$\begin{bmatrix} x_p \\ y_p \end{bmatrix} = \begin{bmatrix} \cos\theta & -\sin\theta \\ \sin\theta & \cos\theta \end{bmatrix} \begin{bmatrix} x'_p \\ y'_p \end{bmatrix}, \tag{2.14}$$

Step 5. The pressure of the liquid reservoir connected to O_1 or O_2 is changed according to the following equation (see, also, Fig. 2.9),

$$P_{O_1} = P_{O_1}^0 + K\left(y_p - y_0\right) \quad \text{if } y < 0,$$
$$P_{O_2} = P_{O_2}^0 + K\left(y_p - y_0\right) \quad \text{if } y > 0, \tag{2.15}$$

here, $P_{O_1}^0$ and $P_{O_2}^0$ are the base pressures, y_0 is the device center on the extensional axis and K is the proportional gain.

Step 6. The pressures in the reservoirs are changed using the NI-DAQ card (Fig. 2.9).
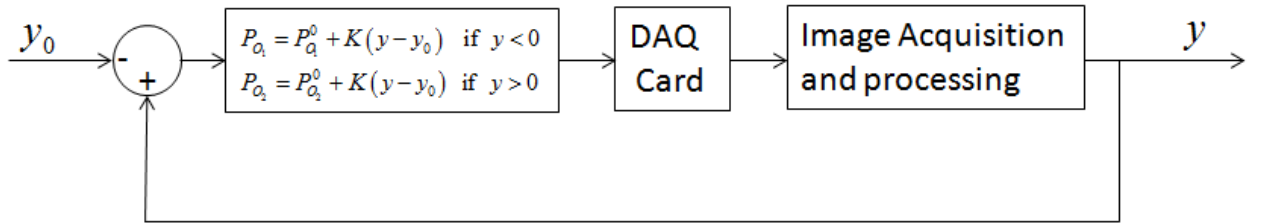
Figure 2.9. Block diagram for proportional control.

2.7 Materials and methods

The materials and methods for the calibration experiments and the particle manipulation experiments with emulsion systems are described below.

2.7.1   Calibration experiments

Materials Used:

Fluorescent beads (Polyscience Inc.), 1 μm in diameter, suspended in glycerol/water (80 wt% glycerol) mixture are used for the device calibration and algorithm testing. Fluorescent particles are used to calibrate the stagnation point position. The stagnation point position is obtained by observing the streamlines formed by the particles by taking long exposure images of the flow field. A high concentration (~1000 particles/μl) of particles is required for a reasonable exposure time. For strain rate calibration, we use a low concentration (~40 particles/μl) of hollow glass beads, 11 μm in diameter in light mineral oil. The low concentration eliminates particle-particle interaction effects. Fluorescent beads, 1 μm in diameter, were also used to demonstrate the ability of the device to control and steer a particle along any pre-defined arbitrary path[1].

While performing the strain rate calibration and particle trapping we used the suspending fluid such that either the density difference between the particle and the suspending medium was small (strain rate calibration experiment) or the suspending fluid viscosity was high. This was required to minimize the gravity induced settling of the particle in the device.

2.7.2   Soft particle experiments

In order to demonstrate the ability of the device to study the dynamics of soft particles, we choose a water-in-oil emulsion as a representative system. Light mineral oil is used as continuous phase. The dispersed phase is 1mM SDS (Sodium dodecyl sulfate) solution. Span® 80 (Sorbitane monooleate), a non-ionic surfactant was added to mineral oil at 0.5% (w/w) to stabilize the water droplets against coalescence. All chemicals were purchased from Sigma-Aldrich and were used without further purification.

---

[1] Here, we have used 1 μm bead but any particle whose position can be accurately determined can be trapped at the device center, for example, a fluorescently labeled DNA molecule (~100 nm) can also be trapped at the device center.

[2] The largest drop which can be trapped at the device center for measuring ultra-low interfacial tensions is limited by the area of constant strain rate and for the present device this value is 300 μm. See sec. 5.1.1 for further

Single drop experiments were performed to study the deformation of drops with increasing strain rate. A theory was developed to estimate interfacial tension between the phases from the drop deformation data.

The water-in-oil emulsion is generated using a T-junction on one of the inlets upstream of the diamond region of the device. The flow rate of water is kept at 1 µl/hr using a syringe pump. The oil is flowed at a pressure differential of 4 psi leading to a flow rate of 26 µl/hr. At these low flow rates, interfacial forces dominates the hydrodynamic stresses [33], and hence, the droplet completely spans the channel width. In this regime, the size of the discrete fluid segment is given by the following relationship.

$$L_s/w = 1 + \alpha \left(Q_{water}/Q_{oil} \right) \tag{2.16}$$

Here, L_s is the length of the slug, w is the channel width, Q_{water} and Q_{oil}, are the flow rates of water and oil, respectively, and α is a constant which depends on the geometry of the T-junction[2]. These drops spanned the channel depth and thus no gravity effects are observed. When a few droplets are formed at the junction, the water flow is cut off and the droplets are brought to the center of the diamond region of the device. One of the droplets is trapped at the device center for an experiment.

2.7.3   Interfacial tension measurement.

The interfacial tension (IFT) between SDS solution and oil was measured with a Texas-500 spinning drop interfacial tensiometer (Temco, Inc., American), with an accuracy of 10^{-6} mN/m. In this method, a drop of oil is injected in a horizontal tube filled with SDS solution. The tube is then spun at a high speed of rotation, ω; this creates a centripetal force and centers the light drop. As ω is increased,   the drop forms an elongated cylinder with spherical caps. The elongation stops when the centrifugal forces are balanced by the interfacial forces. For drops

---

[2] The largest drop which can be trapped at the device center for measuring ultra-low interfacial tensions is limited by the area of constant strain rate and for the present device this value is 300 µm. See sec. 5.1.1 for further improvements in device design to extend this limit.

with length greater than four times the radius, Vonnegut's expression [34] is used to calculate the surface tension.

$$\gamma = \frac{\Delta\rho\omega^2}{4}R^3 \qquad (2.17)$$

Here, γ is the interfacial tension, ω is the rotational velocity, $\Delta\rho$ is the density difference between the heavy and the light phase and R is the radius of the drop. A convenient form of the above equation in the units used by the Texas-500 is as follows:

$$\gamma = 3.42694 \times 10^{-7}\left(\Delta_h - \Delta_l\right)T^2\left(DC_r\right)^3, \qquad (2.18)$$

where, γ is the interfacial tension in mN/m , T is the rotational velocity in rpm, Δ_h is the density of the heavy phase in gm/ml, Δ_l is the density of the light phase in gm/ml, D is the measured drop width in mm and C_r is an experimentally measured correction factor to account for the refraction of the correction factor for refraction due to the tube and the liquid.

Chapter 3

3   Device Calibration and Algorithm Testing

In this chapter, we describe the calibration procedure that establishes the relationships between the applied pressure levels in the inlet and outlet reservoirs, and the stagnation point and the strain rate. The characterization allows us to invoke the correct pressures in the reservoirs to manipulate the positions of particles, and impose known strain rates at the device center for drop stretching and droplet-droplet collision experiments.

3.1   Determination of the device center
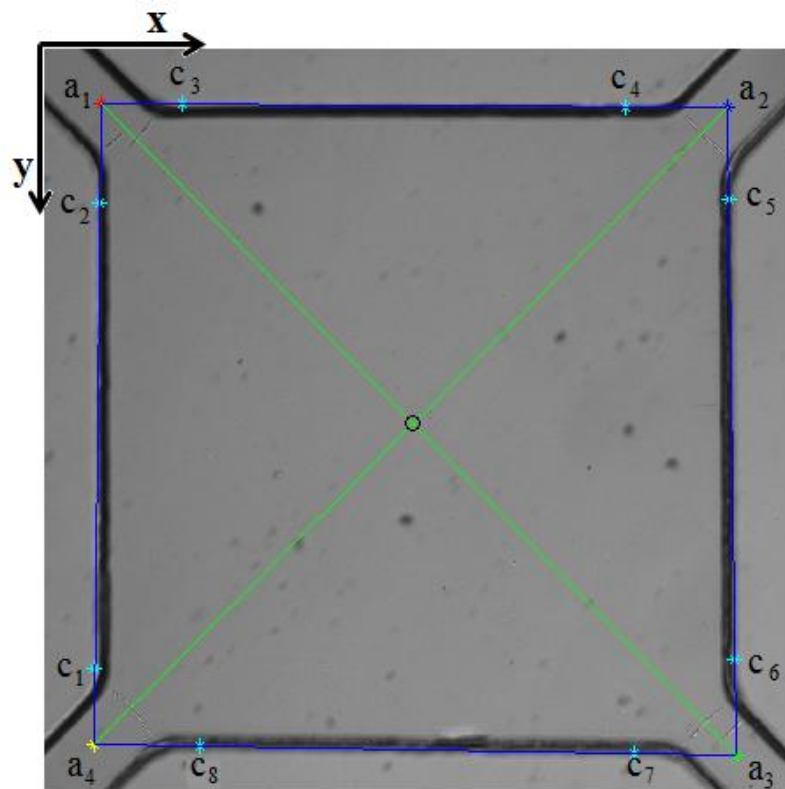
Figure 3.1 Image of a representative device showing the points on the edges, c_i (used to calculate the equation of the edge as shown in Appendix II), the edge intersection points, a_i, the device center, and the orientations of the compressional and extensional axes. For the present

device, the compression and extensional axes are at 44.22^o and 134.49^o from the horizontal, respectively. The device center is at [821.45 µm, 619.14 µm] with respect to the origin at the top left corner and the length of the device edge, between a_1 and a_2, for example, is 980.06 µm.

Before the device calibration and particle trapping experiments can be performed, it is necessary to determine the device center. To achieve this, we take a brightfield image of the device under stagnant conditions. A MATLAB® code then computes the orientation of the extensional and compressional axes, the center of the device and the length of the side of the device. Fig. 3.1 shows the axes orientations, device center and edge length of a representative extensional flow device.

3.2   Flow field calibration.

The flow field calibration involves the determination of the stagnation point and the strain rate for different combinations of inlet and outlet pressures, as described in the following subsections.

3.2.1   Stagnation point calibration

The extensional flow device is photographically investigated in order to relate the stagnation point position to the difference in the inlet and outlet pressures. Long exposure photographs of fluorescent beads, which act as tracer particles, are taken to determine the stagnation point for a series of pressure combinations. Fig. 3.2 shows such exposure images, where the inlet and the outlet pressures are shown. The marker (red dot) in the experimental images shows the position of the stagnation point calculated from the analytical solution (Appendix I). It should be noted that the analytical solution is valid for any arbitrary combination of the flow rates and predicts the stagnation point position quite precisely. Also shown in each subfigure is the flow profile expected from simulations in COMSOL. One can see the agreement between experiment and theory is good, but not perfect. Fig. 3.3 provides a more detailed comparison between the stagnation point position obtained from the analytical solution and the experiments. The maximum error in stagnation point position is 18 µm, which is 1.8% of the device side length. The error in the stagnation point position at the device center is 3 µm.

The mismatch between the analytical solution and the experiments may be due to the fact that there are some imperfections during device fabrication and/or assembly. For example there could be a mismatch in the edge lengths of the device, non-uniformities in the channel depth, and/or unequal resistances in the tubes leading to the device. Such imperfections are evident in the asymmetric pressure combinations that are required to place the stagnation point exactly at the device center. Fortunately, for the experiments performed in this thesis, these errors are tolerable; drops and particles can be trapped at the center for extended periods of time (e.g. see Fig. 3.6). In the future, a model-predictive control scheme will be implemented to make the control loop 'learn' about these imperfections and suitably modify the existing model to account for them.

(a)

(b)

(c)

(d)

(e)
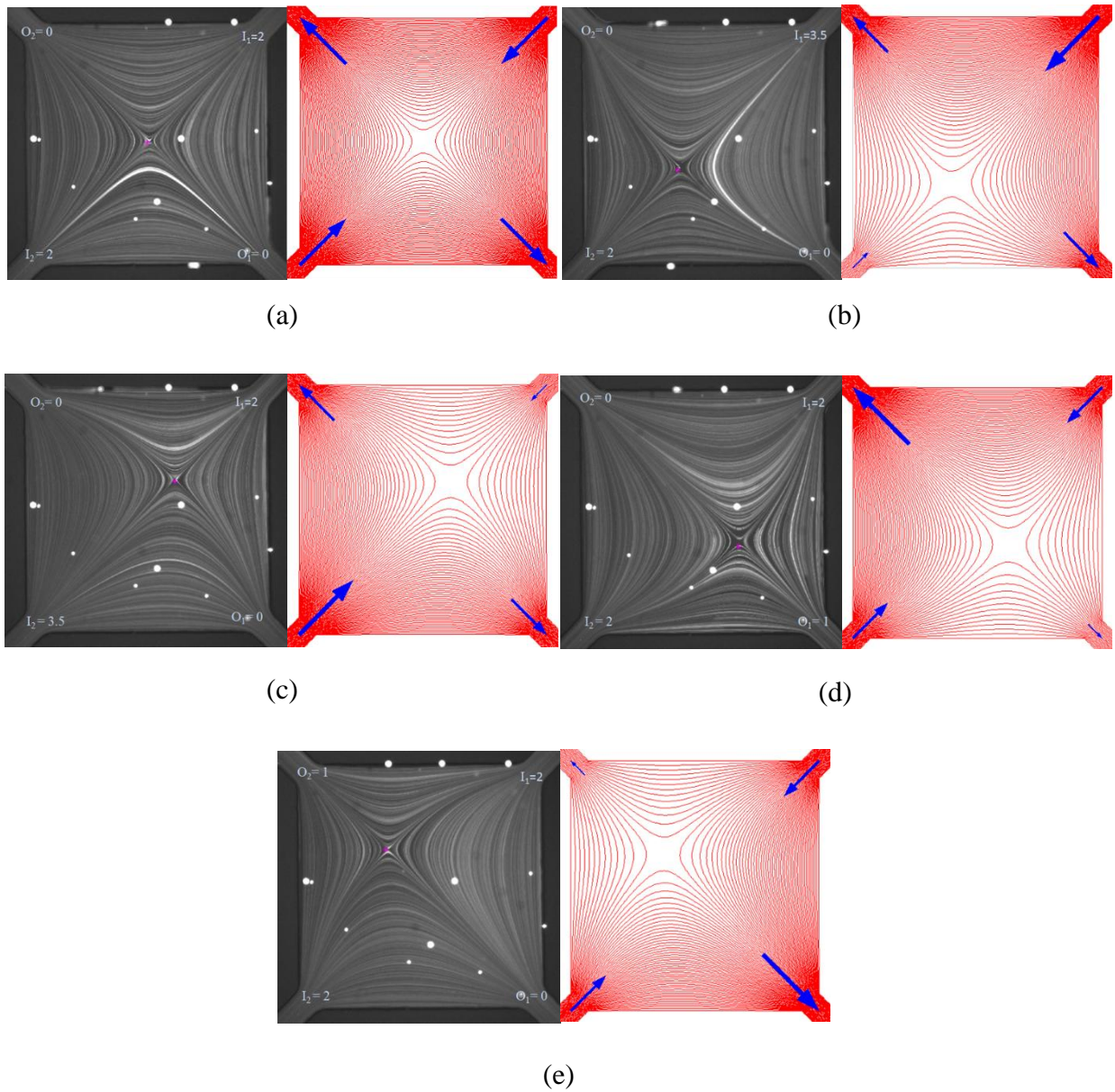
Figure 3.2 Stagnation point position with different inlet and outlet pressure combinations. In each subfigure, experimental streamlines are shown on left, and streamlines simulated in COMSOL for the same pressure combinations are shown on the right. In the experimental pictures, the numbers indicated at the inlets and outlets are the pressures imposed in the reservoirs in units of psig, and the red dots are the locations of the stagnation points.
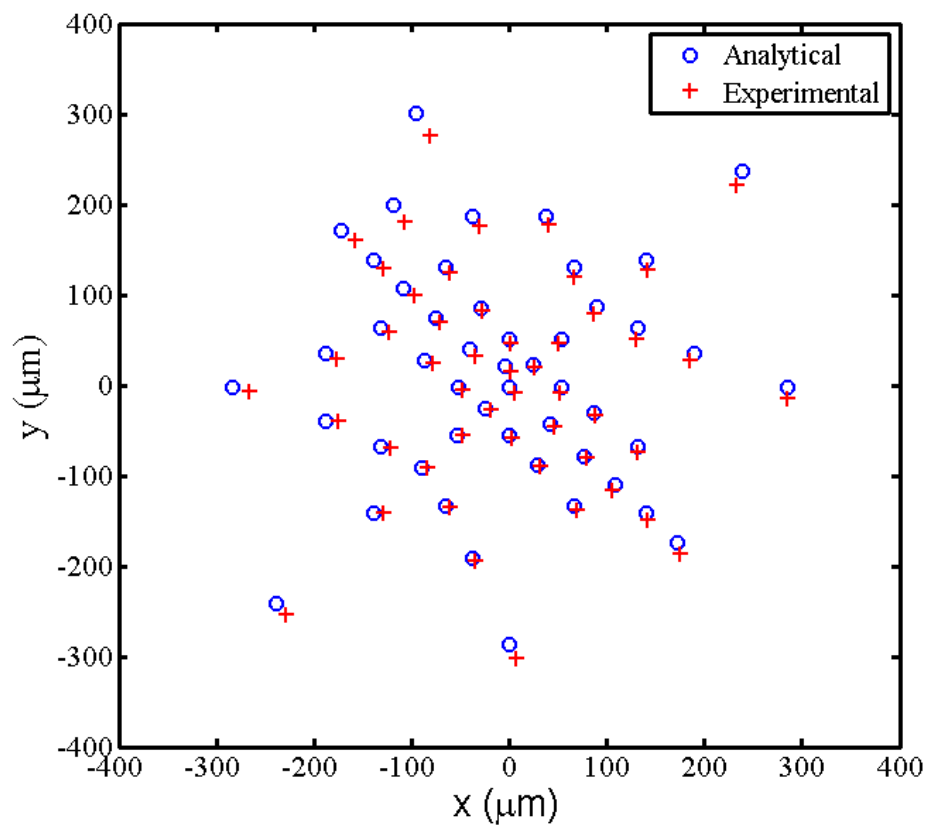
Figure 3.3 Plot showing the error between the stagnation point position obtained by experiments and theory. [o – theoretical predictions, + – experimental data].
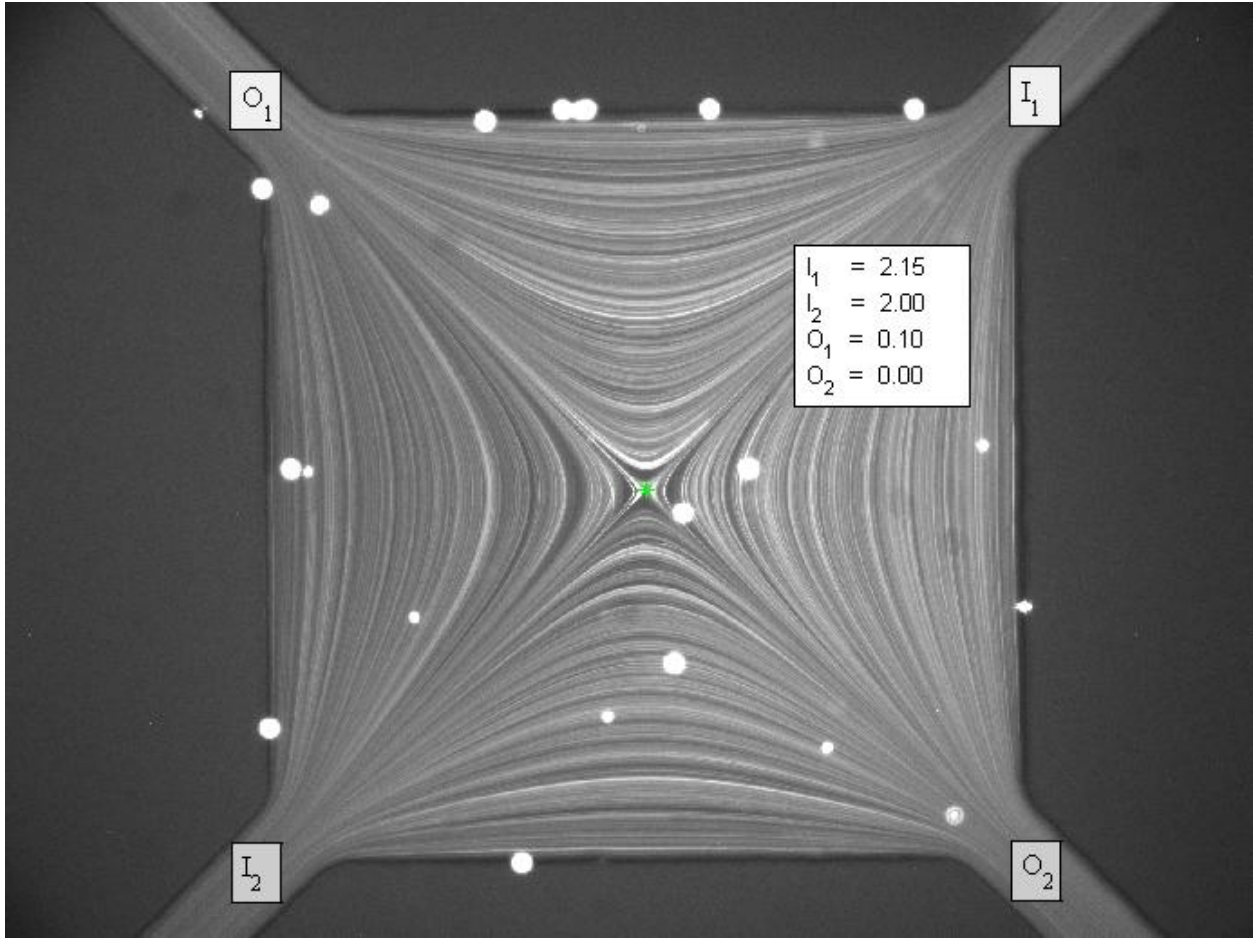
Figure 3.4. Long exposure image showing the pressure combinations for which the stagnation point position is almost exactly at the device center.

3.2.2   Strain rate Calibration.

From Eq. 2.1, we know that when the stagnation point is located at the device center, which occurs for the same flow rate Q in each port of the device, the strain rate at the stagnation point is directly proportional to the liquid flow rate entering or leaving the slot.

However, from Eq. 2.3, equal flows in each channel imply that Q is proportional to the pressure difference, ΔP, between an inlet and outlet reservoir,

$$Q = \frac{1}{2} \frac{\Delta P}{R},$$

(3.1)

rendering the strain rate to be directly proportional to the pressure drop, ΔP. Thus

$$G = \frac{k_d}{4bW^2R}\Delta P = K\Delta P, \tag{3.2}$$

where

$$K = \left(\frac{k_d}{2bW^2R}\right)\left(\frac{1}{2R}\right). \tag{3.3}$$

The adjustment of the pressure differential thus provides a way to controllably modify the linearly dependent strain rate.

In order to determine the relationship between G and ΔP, a suspension of hollow glass beads is introduced in the device at a set pressure differential. A video of the flowing suspension in the slot is taken and position of the glass beads ascertained with time is evaluated by analyzing each frame of the video. Only the frames where the glass beads are closer than 100 μm from the device center were analyzed. Since the flow field is linear in strain rate near the stagnation point, the following equations, are used to calculate the strain rate for a set pressure differential.

$$\begin{aligned} x &= x_0 \exp\left[-G(t-t_0)\right], \\ y &= y_0 \exp\left[G(t-t_0)\right]. \end{aligned} \tag{3.4}$$

Here, x and y are the position at a given time t. x_0 and y_0 are the particle position at time t_0 initial particle positions

An alternative, easier way of obtaining K [Eq.(3.2)] is to measure the flow rates entering the individual arms of the channel for fixed pressure differentials between the inlet and outlet reservoirs. This would yield the proportionality constant, $1/2R$ in [Eq. (3.1)] Since we already know via a COMSOL simulation the relationship between the strain rate at the stagnation point and the inlet/outlet flow rate (i.e. we know the constant k_d in [Eq. (3.2)], the strain rate can be connected to the pressure drop via Eq. (3.1). This is a semi-empirical way of determining K.
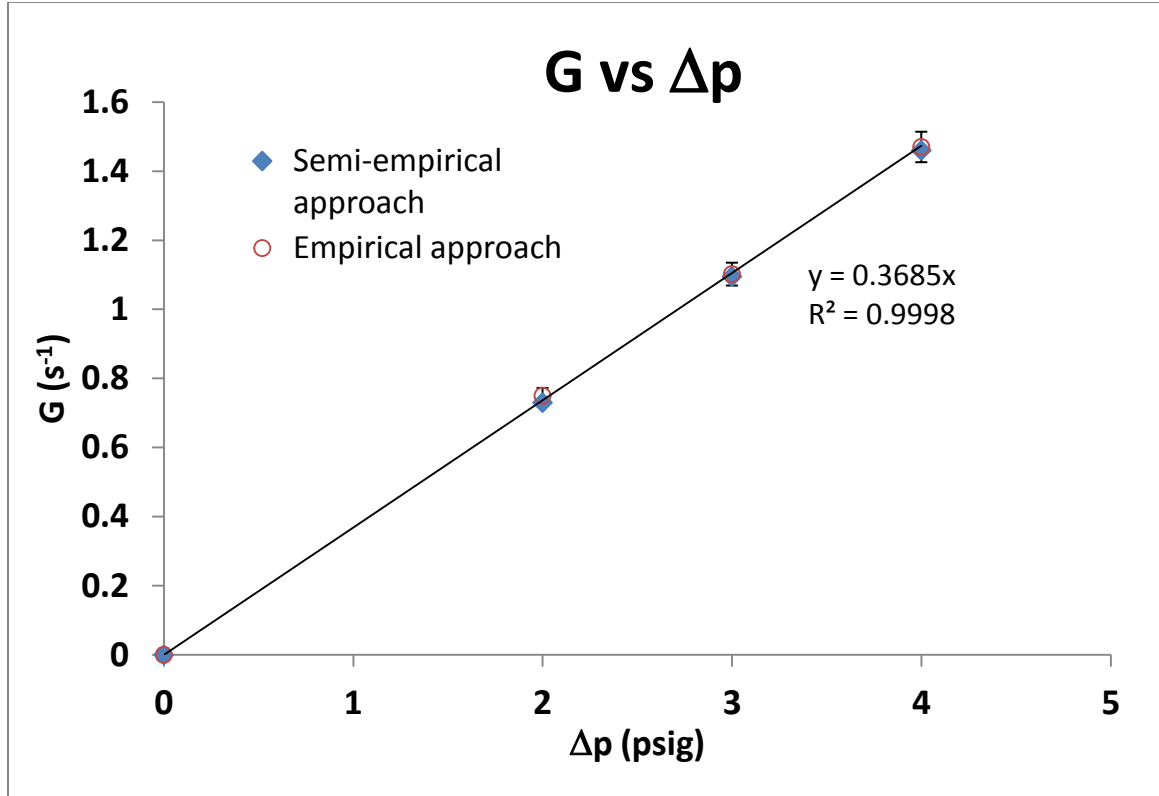
Figure 3.5 Strain rate obtained from the empirical and semiempirical methods for different pressure differentials between inlets and outlets.

Fig. 3.5 shows the strain rate versus the pressure difference between the inlets and the outlets. One can see that the two methods are both linear and in excellent agreement.

3.3 Particle trapping at the device center

With the stagnation point position calibrated, the trapping of a single fluorescent particle can be implemented. In order to control the particle, fluid flow is started by manually adjusting the pressures, such that a particle is visible along any diagonal of the device. The pressure differential is chosen such that the flow velocities are not high, due to two reasons. First, at high velocities, if the particle is caught along the extensional flow diagonal, it is swept away extremely quickly to the outlet due to the exponentially increasing separation from the stagnation point with time. This leaves minimal human reaction time to perform the manual operation of bringing the particle close to the center. Second, at high velocities, the strain rates are large,

which could lead to breakup of soft particles; this is to be avoided. Once the particle is spotted in the diamond slot, the control is shifted to automatic control via the control scheme outlined in chapter 2, and the particle is steered towards the center of the device by manipulating the stagnation point position along the extensional axis.

The fluctuation of the particle position around the stagnation point is shown in Fig. 3.6. The mean error is 3.6 μm, and the standard deviation in error is 0.2 μm. It should be noted that the resolution of the image obtained from the camera is 1 μm/pixel and the reported standard deviation is 0.2 mm which is less than the minimal resolution. We report this smaller value as we perform a cubic spline fit to the intensity data of the image and the maximum of the spline function is assumed to be the particle position and thus standard deviation of sub-micron level are possible [28].
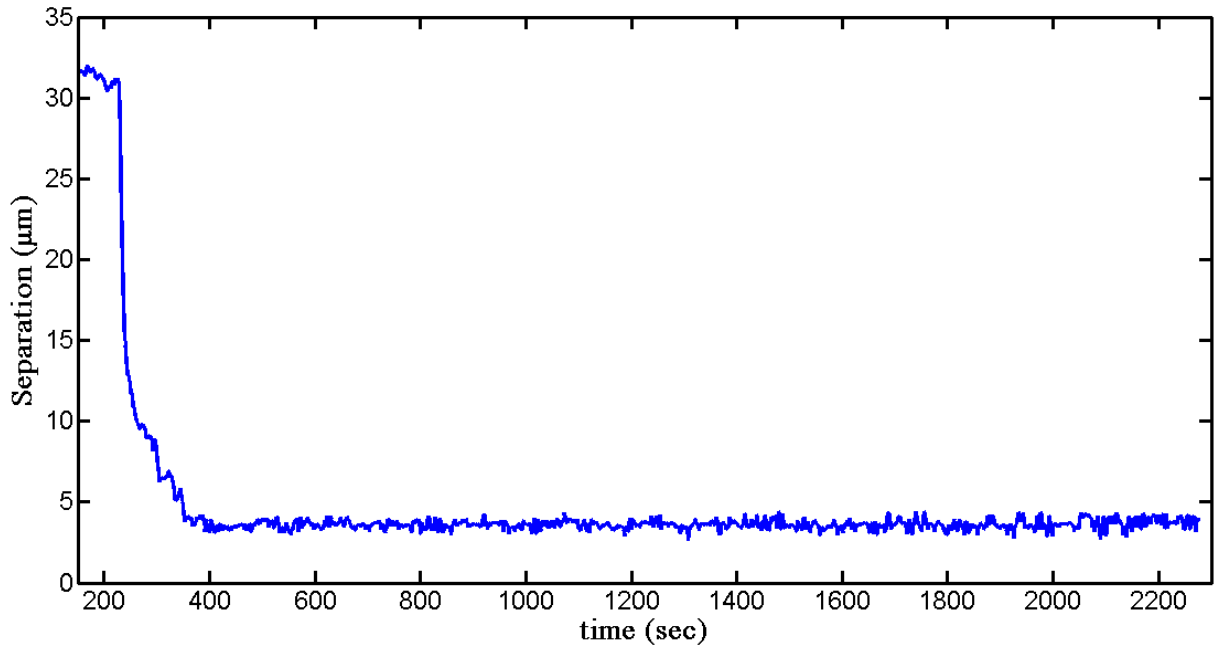
Figure 3.6. Separation between the particle position and device center with respect to time.

3.4 Particle trapping at an arbitrary position and manipulation of a particle along a predefined path.

In order to trap a particle at any arbitrary position in the diagonal, the flow rates ratio through the inlets and outlets required to bring the stagnation point at that position is calculated using the analytical solution (see Appendix I). The pressures combination required to position the stagnation point at the desired arbitrary location are then calculated using Eq. 2.4-2.6.

Now, the distance of the particle position from the desired trapping position along the extensional and compressional axis are calculated and the particle is controlled via the control scheme outlined in chapter 2. The fluctuation of the particle around an arbitrarily-defined desired position is shown in Fig. 3.7. The mean error in particle position is 1.1 μm and the standard 0.5 μm.

With the ability to trap a particle at any arbitrary position in the diamond, we demonstrate two-dimensional manipulation of particles by steering a single particle along a predefined path. A particle is first trapped at the device center (sec 3.2). Once the distance between the particle position and device center is below a threshold, the manipulation of particle along a predefined path is started.
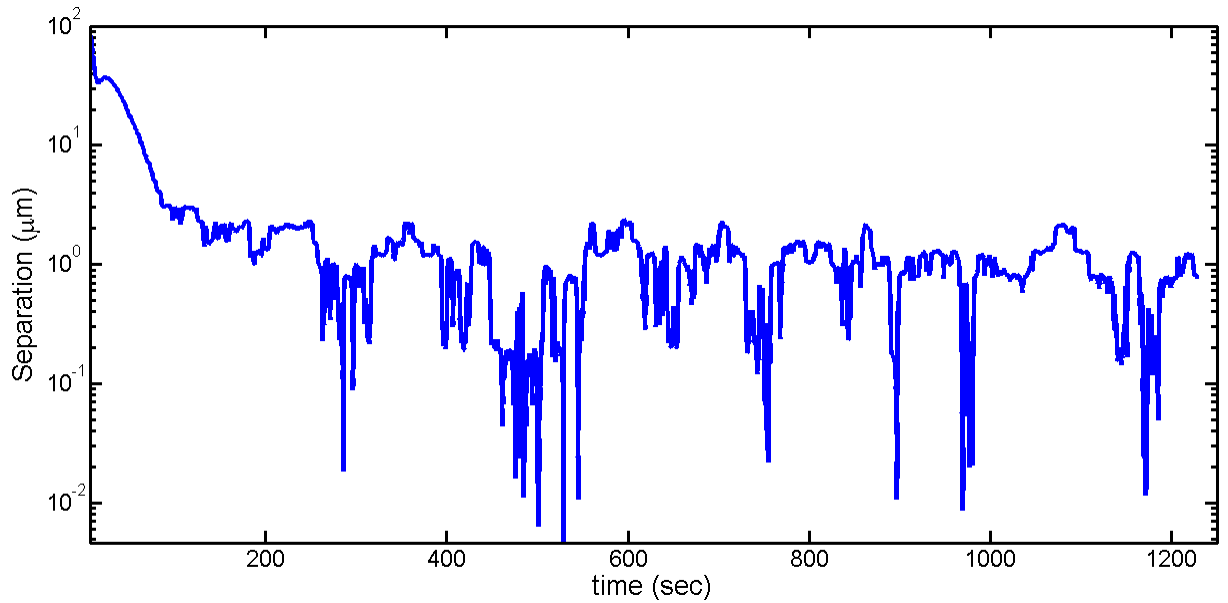
Figure 3.7 Error between the particle position and new trapping position with respect to time.

The particle path is divided into a fixed number of points. The particle is then steered towards the starting point of the path by changing the trapping position to the starting point. Once the distance between the particle position and the trapping point is below the threshold the trapping

position is updated to the next point along the path. This seqence is continued for all points on the path. Fig. 3.8 shows the trajectory taken by a particle when the predefined path is a cardioid
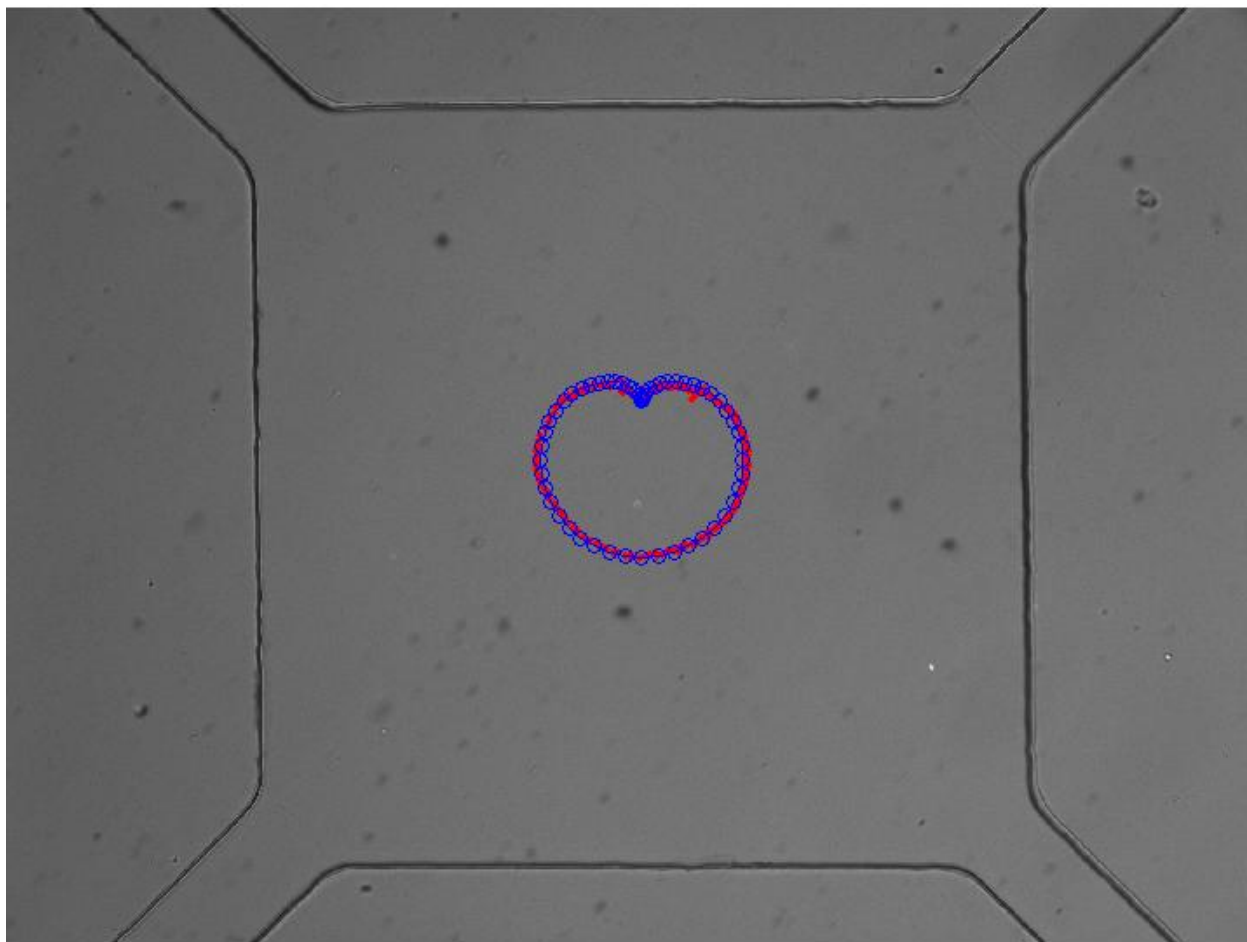
Figure. 3.8 Trajectory of a particle using particle trapping. The red curve shows the particle path. The blue circles show the predefined particle path, a cardioid.

Chapter 4

4 Evaluation of Interfacial Tension With The Extensional Flow Device

To demonstrate the capabilities of the extensional flow device to study soft particle dynamics, we show that the device can be used to study the stretching of a drop in a confined extensional flow. In particular, we determine the interfacial tension of a water-in-oil system using our device.

4.1 Theory

The theory relating the drop deformation, strain rate and the interfacial tension is developed for small deformations of the drop from its initial unperturbed equilibrium shape.

4.1.1 Problem definition and governing equations
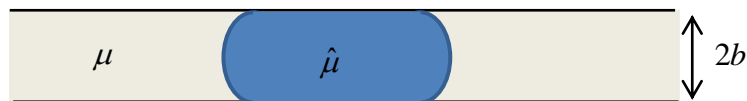
(a)
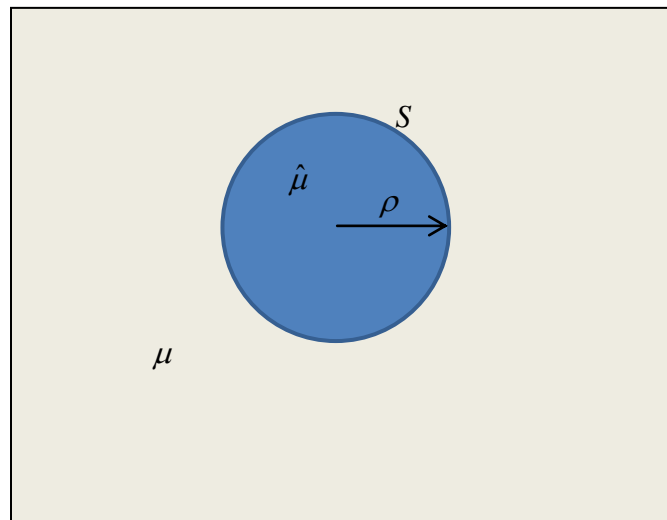
(b)

Figure 4.1. Schematic of a squeezed drop. (a) side view of the channel. (b) Top view of the channel.

Consider a drop of viscosity $\hat{\mu}$ suspended in a fluid of viscosity μ, and squeezed between two plates separated by a constant distance, $2b$ (see Fig. 4.1). The interfacial tension between the two fluids is γ. In the absence of flow, let the radius of the circle traced by the edge of the squeezed drop be ρ. The cylindrical co-ordinate (r, θ) system is employed here, with the origin as the center of the drop. The shape of the edge of the interface, S, as viewed in the x - y plane, is assumed to be of the form

$$r = \rho\left[1 + f\left(\theta, t\right)\right] \tag{4.1}$$

f, represents the dimensionless deviation of the shape from a circle, the equilibrium shape.

Here we examine the deformation of the drop in the limit of large drop radii relative to the depth of the channel (i.e. R $>>$ b), or the Hele-Shaw limit. Although the velocity field is, in general, fully three-dimensional, it is known that in the Hele-Shaw limit, the velocity in the z direction is much weaker than the velocities in the x and y directions. Therefore, we will ignore the z component, and any vector field employed (velocities, normals, tangents) henceforth will imply a two-dimensional field in the x-y direction.

In the Hele-Shaw limit, the depth-averaged suspending-fluid velocity field, $\mathbf{u}$, is given by

$$\mathbf{u} = -\frac{b^2 \nabla p}{3\mu}, \tag{4.2}$$

where the pressure field, p, obeys the harmonic equation

$$\nabla^2 p = 0. \tag{4.3}$$

The governing equation for the depth-averaged drop-fluid velocity field, $\hat{\mathbf{u}}$, is

$$\hat{\mathbf{u}} = -\frac{b^2 \nabla \hat{p}}{3\hat{\mu}}, \tag{4.4}$$

The drop-fluid pressure field, $\hat{p}$, is also a harmonic.

$$\nabla^2 \hat{p} = 0. \tag{4.5}$$

4.1.2 Boundary conditions

The specific ambient field considered here is a linear extensional flow, $\mathbf{u}_\infty$, given by

$$\mathbf{u}_\infty = -\frac{b^2 \nabla p_\infty}{3\mu} \tag{4.6}$$

where, the ambient pressure field, p_∞, is

$$p_\infty = -\frac{3\mu G}{2b^2} \mathbf{x} \cdot \mathbf{E} \cdot \mathbf{x} = -\frac{3\mu G}{2b^2} r^2 \cos 2\theta, \tag{4.7}$$

The tensor $\mathbf{E}$ is the symmetric rate of strain tensor, which is equal to [1 0; 0 -1] for the linear extensional flow considered here. The boundary condition for the internal velocity field is that it is finite (i.e. does not diverge).

The continuity of the normal velocity across the interface requires

$$\mathbf{u}\big|_S \cdot \mathbf{n} = \hat{\mathbf{u}}\big|_S \cdot \mathbf{n} \tag{4.8}$$

The normal stress balance across the interface becomes, to leading order,

$$\hat{p} - p = \gamma \kappa, \tag{4.9}$$

Here, γ is the interfacial tension, and the curvature, κ , is given by

$$\kappa = \frac{(1+f)^2 + 2f'^2 - (1+f)f''}{\rho \left[(1+f)^2 + f' \right]^{3/2}}. \tag{4.10}$$

The edge of the drop propagates according to the kinematic condition

$$\frac{\partial f}{\partial t} = \hat{\mathbf{u}}\big|_s \cdot \nabla\left[\frac{r}{\rho} - (1+f)\right].$$ (4.11)

4.1.3 Solution

The analytical solution developed here is for small capillary numbers, i.e

$$\mathrm{Ca} = \frac{\mu G \rho^3}{\gamma b^2} \ll 1.$$ (4.12)

In this limit, the drop deformation is small, and the shape of the drop can be regarded as a small perturbation from a circle, i.e. $f \ll 1$ (see Eq.(4.1)). Thus, the equilibrium shape of the drop can be computed by performing calculations of the velocity and pressure fields for a circular edge.

The solutions for the velocity and pressure fields for a circular edge, subject to the ambient boundary conditions (4.6) and (4.7) are

$$p = -\frac{3G\mu}{2b^2}\mathbf{x}\cdot\mathbf{E}\cdot\mathbf{x} + c_1\frac{\mathbf{x}\cdot\mathbf{E}\cdot\mathbf{x}}{r^4},$$ (4.13)

and

$$\mathbf{u} = -\frac{b}{3\mu}\left[-\frac{3G\mu}{b^2}\mathbf{E}\cdot\mathbf{x} + c_1\left(-4\frac{\mathbf{x}\cdot\mathbf{E}\cdot\mathbf{x}}{r^6}\mathbf{x} + 2\frac{\mathbf{E}\cdot\mathbf{x}}{r^4}\right)\right],$$ (4.14)

for the suspending fluid, and

$$\hat{p} = \hat{p}_0 + c_2\,\mathbf{x}\cdot\mathbf{E}\cdot\mathbf{x},$$ (4.15)

and

$$\hat{\mathbf{u}} = -\frac{b^2}{3\hat{\mu}}\left(2c_2\,\mathbf{E}\cdot\mathbf{x}\right),$$ (4.16)

for the drop fluid. $\hat{p}_0$ is a base, excess pressure that exists within the drop even under quiescent conditions due to the Laplace pressure difference across the interface between the two fluids. c_1

and c_2 are constants that can be determined by the application of the remaining boundary conditions [Eq. (4.8) and Eq. (4.9)].

The definition of the normal vector for a circle is simply the radial vector.

$$\mathbf{n} = \frac{\mathbf{x}\big|_S}{\rho}.$$ (4.17)

To match the normal component of the velocity at $r = \rho$, we require

$$\frac{c_1}{\rho^4} + \frac{c_2}{\lambda} = \frac{3\mu G}{2b^2}.$$ (4.18)

Applying the normal stress balance in Eq. (4.9) requires the curvature of the interface, κ. For small deformations, κ in Eq.(4.9) reduces to

$$\kappa \approx \frac{1}{\rho} - \frac{f + \left(d^2 f / d\theta^2\right)}{\rho}.$$ (4.19)

The normal stress balance Eq.(4.9) simplifies to

$$\left[c_2 - \left(-\frac{3\mu G}{2b^2} + \frac{c_1}{\rho^4}\right)\right]\mathbf{x} \cdot \mathbf{E} \cdot \mathbf{x} = -\gamma \frac{f + \left(\partial^2 f / \partial\theta^2\right)}{\rho}.$$ (4.20)

Note that we have set $\hat{p}_0 = \gamma/\rho$. Examining the forms of the velocity and pressure fields, the deviation in the shape, f, can assume only one form:

$$f = \frac{c_3}{R^2} \mathbf{x} \cdot \mathbf{E} \cdot \mathbf{x}.$$ (4.21)

Since $\mathbf{x} \cdot \mathbf{E} \cdot \mathbf{x} = r^2 \left(\cos^2 \theta - \sin^2 \theta\right) = r^2 \cos 2\theta$, the expression $f + \left(\partial^2 f / \partial\theta^2\right)$ when evaluated at the surface becomes

$$f + \frac{\partial^2 f}{\partial\theta^2} = \frac{c_3}{\rho^2}(1-4)\mathbf{x} \cdot \mathbf{E} \cdot \mathbf{x} = -3\frac{c_3}{r^2}\mathbf{x} \cdot \mathbf{E} \cdot \mathbf{x}.$$ (4.22)

Thus, Eq. (4.18) simplifies to

$$\frac{c_1}{\rho^4} - c_2 = -3\gamma \frac{c_3}{\rho^3} + \frac{3\mu G}{2b^2}. \tag{4.23}$$

Equations (4.18) and (4.20) represent two simultaneous equations in c_1 and c_2, which can be solved to yield these constants as

$$c_1 = -\frac{3\gamma}{(\lambda+1)\rho^3} c_3 - 3\frac{(\lambda-1)}{(\lambda+1)} \frac{\mu G}{b^2}, \tag{4.24}$$

$$\text{and,} \quad c_2 = -\frac{3\gamma\lambda}{(\lambda+1)\rho^3} c_3 - 3\frac{\lambda}{(\lambda+1)} \frac{\mu G}{b^2}. \tag{4.25}$$

Here λ is the ratio of the drop viscosity to the suspending fluid viscosity. The knowledge of these constants completely defines the pressure and velocity fields in terms of the unknown shape constant, c_3.

To determine the shape constant, c_3, we invoke the kinematic condition (4.11), which, for small deformations, reduces to

$$\frac{\mathbf{x} \cdot \mathbf{E} \cdot \mathbf{x}}{\rho^2} \frac{\partial c_3}{\partial t} = \hat{\mathbf{u}}\Big|_S \cdot \frac{\mathbf{x}}{\rho^2}. \tag{4.26}$$

Substituting for $\hat{u}\big|_S$ from Eq. (4.16) simplifies Eq. (4.26) to

$$\frac{\partial c_3}{\partial t} = -\frac{2b^2 c_2}{3\hat{\mu}}. \tag{4.27}$$

Using the expression for c_2 in Eq.(4.27), one gets

$$\frac{\partial c_3}{\partial t} = -\frac{1}{t_c}(c_3 - \text{Ca}), \tag{4.28}$$

where Ca is the capillary number defined in Eq.(4.12), and t_c is the time scale

$$t_c = \frac{\mu(\lambda+1)\rho^3}{2b^2\gamma}.$$

(4.29)

The solution to the ODE in Eq. (4.28) with the initial condition of $c_3\big|_{t=0} = 0$ is

$$c_3 = \mathrm{Ca}\left[1 - \exp\left(-\frac{t}{t_c}\right)\right].$$

(4.30)

The shape of the drop as a function of time is, therefore,

$$r = \rho\left\{1 + \mathrm{Ca}\left[1 - \exp\left(-\frac{t}{t_c}\right)\right]\cos 2\theta\right\}.$$

(4.31)

At steady state, the shape of the drop is given by

$$r = \rho\{1 + \mathrm{Ca}\cos 2\theta\},$$

(4.32)

which is an ellipse with a ratio of major to minor axes of

$$\frac{L}{B} = \frac{1+\mathrm{Ca}}{1-\mathrm{Ca}}.$$

(4.33)

The deformation parameter, D, defined as

$$D = \frac{L-B}{L+B},$$

(4.34)

becomes

$$D = \mathrm{Ca} = \frac{\mu\rho^3}{\gamma b^2}G.$$

(4.35)

Thus, the deformation parameter D should be proportional to the strain rate G, with a proportionality factor, m, given by

$$m = \frac{\mu\rho^3}{\gamma b^2}.$$

(4.36)

Eq. (4.35) will be used to interpret the experimental data in section 4.2.

4.2   Experimental results

4.2.1   Ultralow interfacial tension measurement

A droplet of 1mM SDS solution in mineral oil (0.5 % Span-80) is created in an inlet upstream of the diamond region of the device. The drop is then trapped at the device center. The strain rate is gradually increased and the droplet shape is recorded for every step increase in strain rate. Since, the characteristic time for drop shape evolution for the system studied is O (0.1 s) and the time step between successive changes in strain rate is O(10 s); hence the recorded droplet shape is always at steady state. Fig. 4.2 shows the images of the steady state drop shape at various pressure difference.

(a)   (b)   (c)   (d)   (e)
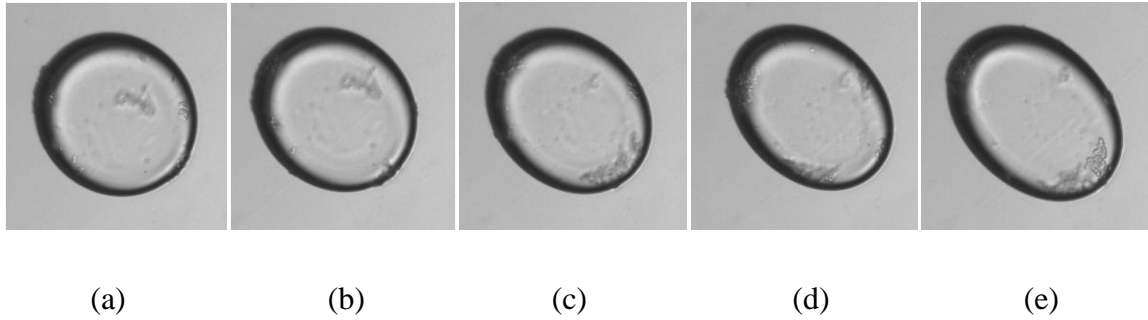
Figure 4.2. Equilibrium shapes of the drop for various pressure differences between the inlet and outlet. (a) 1.0 psi, (b) 1.5 psi, (c) 2.0 psi, (d) 2.5 psi, (e) 3.0 psi. The un-deformed drop radius is 90 μm. Half depth of the extensional flow device, b, is 47 μm.

The major and the minor axes, and hence the deformation, D is obtained from the equilibrium drop shapes. Table 4.1 shows, length of the major and minor axes of the drop, the deformation parameter for various values of strain rates. The strain rates were obtained from the pressure differences using the calibration in sec 3.2.2.

Table 4.1 Drop deformation for various inlet and outlet pressure differences for 1mM SDS solution and Mineral oil (0.5% Span-80) system.

Pressure Difference (psi)	Strain Rate (1/s)	Major Axis length (µm)	Minor Axis length (µm)	Deformation, D
1.0	0.365	189.71	174.17	0.043
1.5	0.547	194.25	169.63	0.068
2.0	0.730	198.74	162.44	0.100
2.5	0.912	203.64	156.27	0.132
3.0	1.095	207.28	151.89	0.154

Fig. 4.3 shows the plot of deformation and strain rate. The slope of the line is used to calculate the interfacial tension using the following equation, derived from the definition of m in Eq. (4.36)..

$$\gamma = \frac{\mu \rho^3}{mb^2} = \frac{0.033 \times \left(91 \times 10^{-6}\right)^3}{0.1385 \times \left(47 \times 10^{-6}\right)^2} = 81.3\,\mu\text{N/m} \tag{4.37}$$
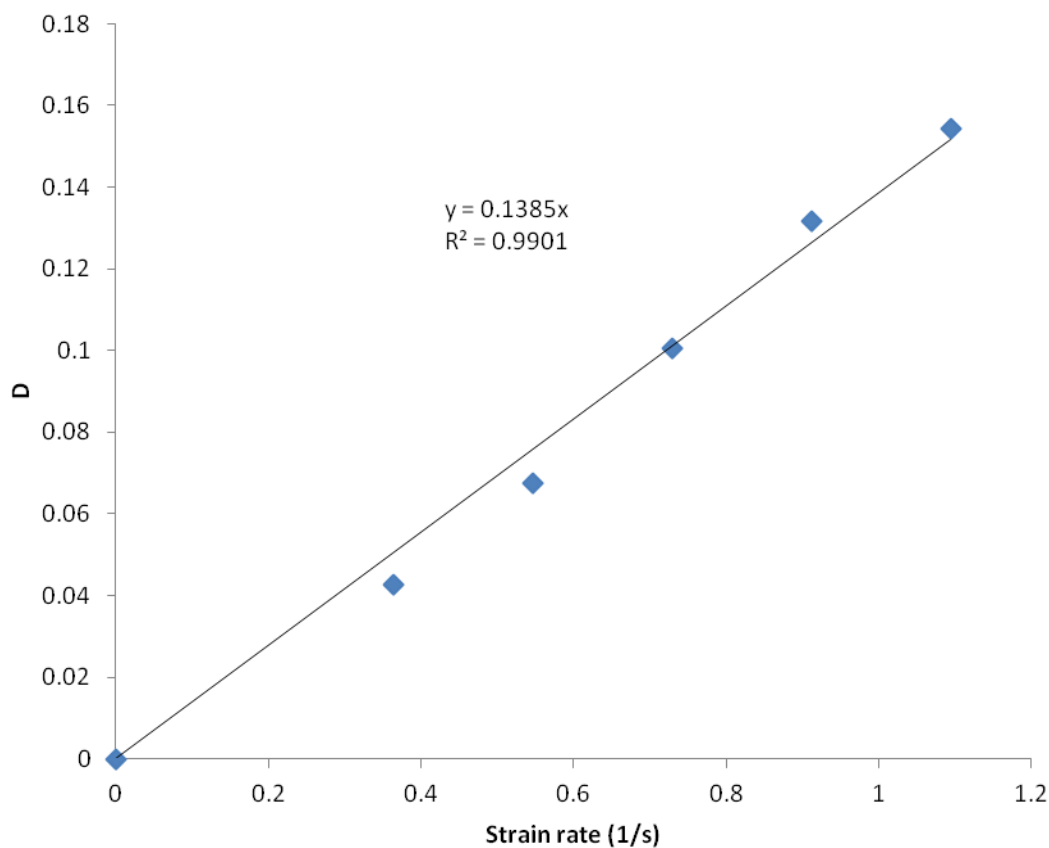
Figure 4.3 Plot showing the drop deformation versus the strain rate. Slope of the line is used to calculate the interfacial tension.

To corroborate the value of measured interfacial tension, the spinning drop tensiometer is also used to calculate the interfacial tension (see 2.7.3). Fig. 4.4 shows a plot of the square of the rotation in RPM against the cube of the inverse of drop diameter.
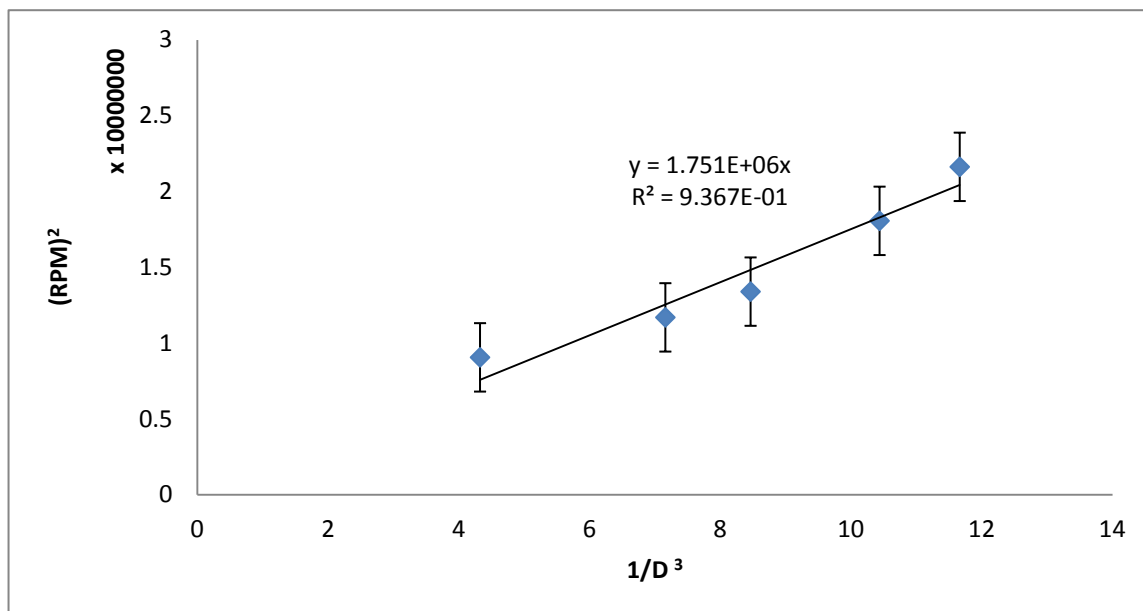
Figure 4.4. Plot of the square of rotation speed versus the cube of the inverse of drop diameter.

The interfacial tension is directly proportional to the slope of the line and is calculated using Eq. (2.18)

$$\begin{aligned}
\gamma &= 3.42694 \times 10^{-7} \times \left(\Delta_h - \Delta_l\right) \times slope \\
&= 3.42694 \times 10^{-7} \times (1 - 0.86) \times 1.751 \times 10^6 \\
&= 8.40 \times 10^{-2}\,\text{mN/m} = 84.0\,\mu\text{N/m}
\end{aligned} \tag{4.38}$$

This value agrees well with the interfacial tension measured using our device.

Chapter 5

5   Avenues for Improvement of The Device And Future Work

In this section, we point out some avenues for improving the performance of the device, and discuss future work that will be undertaken with it.

5.1   Improvement of the device

5.1.1   Geometry of the device
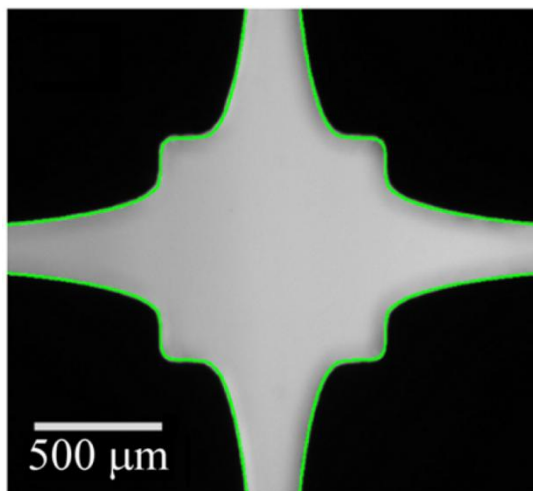
Figure 5.1. The optimum channel shape for 2-D flow (flow invariant in the depth direction) as calculated by [35]

The geometry that we have chosen for the device is a diamond-shaped geometry, which is different from many earlier publications that have adopted a square slot. The choice of this shape was dictated by the availability of an analytical solution for the flow field and stagnation point for arbitrary combinations of the inlet and outlet rates. It was also shown that for given initial flow and strain rates, the diamond shape also provides a 42% greater area of the slot where the strain rate is fairly constant. Although the latter is a good reason to use the diamond geometry, it prompts the question: is this the geometry that can provide the largest area of constant strain rate?

This question has been considered recently [35] but for 2-D flows invariant in the depth direction of the channel. They proposed the channel shape shown in Fig. 5.1, which is essentially a combination of the diamond and the square cross slots. However, our flow geometry is a Hele-Shaw flow, not a 2-D flow. The flow is not invariant in the depth; rather, it is a parabolic flow whose strength is dependent on the local pressure gradient. It is not clear, therefore, whether the optimized geometry in the Hele-Shaw case will also be the shape in Fig. 5.1.

In future work, we will perform this optimization. Our optimization problem is, in fact, simpler, because we need to solve only for the potential flow equations instead of the complete creeping flow equations. Experiments will be performed in the optimized, Hele-Shaw geometry. The stagnation points and the strain rates required for the code as functions of the flow rates in the various ports will be computed in COMSOL, and stored in the form of interpolation tables that can be invoked by the control code.

5.1.2   Control loop time

It is highly desirable that the control loop time be as short as possible, as it is this time that limits the highest strain rate of operation. Currently, the four steps in this control loop, along with their typical times in milliseconds are   1. capture of the image into MATLAB (10 ms); 2. image analysis to yield the center of the particle ($\approx$200 ms); 3. calculation of the pressures required to be imposed on the four reservoirs (less than 10 ms); and 4. instructing the pressure controllers through the DAQ card to impose the pressures ($\approx$ 20 to 70 ms). The total time consumed in one loop of the iteration is, thus, about 300 ms. Clearly, the rate-determining step in this process is image analysis step. Since the frame rate of the camera (RETIGA-2000R) at the employed resolution (1600 x 1200, necessary for accurate determination of the particle center, particularly for fluorescent beads) is 7.5 fps, the rate at which frames are delivered [sub-step (a)] is 150 ms per frame. We believe that this time can be reduced by adjusting the control code to acquire a specific region of interest of the image, instead of the entire image. For the images required for the experiments discussed in chapter 4, the image size required is at least 500 x 500. This has to be implemented conditionally and carefully in the code, as the positions of the particle center and stagnation points have to be modified depending on the size of the image acquired during the control process. We believe that with this adjustment, the control loop time can be reduced to about 70 ms, which is a factor of 4 faster than the current code.

5.1.3   Limitation on the stress applicable on the soft particle

To induce flow in the channels, we use pressure-controlled reservoirs. The maximum pressure rating of the pressure controllers is ΔP_{max} = 5 psi. This pressure limits the flow rates in the channels, and, in turn, the maximum stress that may be imposed on a particle in the slot. As discussed in chapter 3, the flow rate in each channel is inversely related to the resistance R in the tubing preceding the channel, and the maximum strain rate that may result is (c.o Eq. 3.2)

$$G_{max} = \frac{k_d}{2bW^2R}\Delta P_{max}. \tag{4.39}$$

The resistance R is proportional to the viscosity of the fluid, μ, since the Reynolds numbers of the flow are small. Thus,

$$R = R_0\mu, \tag{4.40}$$

and
$$G_{max} = \frac{k_d}{2\mu bW^2R_0}\Delta P_{max} \tag{4.41}$$

The tube resistance R_0 is picked on the basis that it is a factor of ζ (about 10) greater than the resistance in the rectangular microfluidic channels leading up to the extensional flow slot. Therefore,

$$R_0 = \zeta\frac{3L}{2b^3w}. \tag{4.42}$$

Here, L is the length of the entrance channel, and W is its width. Substituting (4.42) in (4.41) , we have

$$G_{max} = \frac{k_d b^2 w}{3\mu\zeta W^2 L}\Delta P_{max}. \tag{4.43}$$

Now that we have the expression for the maximum possible strain rate in the slot, we can predict the maximum stress, τ_{max}, that may be imposed on a particle in the slot.

$$\tau_{max} = \mu G_{max} = \frac{1}{3\zeta}\left(\frac{w}{L}\right)\left(k_d \frac{b^2}{W^2}\right)\Delta P_{max}. \tag{4.44}$$

One can see that τ_{max} is proportional to ΔP_{max}, inversely related to the factor ζ, proportional to the aspect ratio b/W, dependent on the geometrical factors k, w & L, and *independent of any fluid property*, including the viscosity of the fluid.   Thus, it does not depend on what (Newtonian) fluid is being used in the experiment. For typical experimental parameters: $k = 10$, $w = 100~\mu$m, $W = 1$ mm, $b = 50~\mu$m, $L = 1$ mm, and $\zeta = 10$, τ_{max} turns out to be about 3 Pa for ΔP_{max} = 5 psi.   If we are analyzing the deformation of a drop with a radius of $\rho = 100~\mu$m and an interfacial tension of $\gamma = 10$ mN/m, we get a maximum capillary number of

$$Ca_{max} = \frac{\tau_{max}\rho^3}{b^2\gamma} = O(0.1). \tag{4.45}$$

This is enough to stretch the drop, but not to break it, since capillary numbers of $O(1)$ are typically required for breakup. Therefore, with the current setup, we anticipate that we will not be able to break the drop with high tensions at the constant strain rates near the device center[3]. But such stresses are ideal for investigating breakup processes for drops with low to ultralow interfacial tensions ($\gamma = 1$ mN/m to 10^{-3} mN/m).

Since the slot aspect ratio , W/b, and the resistance factor, ζ, cannot be decreased in order to maintain a Hele-Shaw flow and to allow particle control (see chapter 2), respectively, the only geometric factors that we can really change to accommodate higher stresses at the given maximum pressure drop are W and L.   These parameters influence the resistance of the

---

[3] If the production of smaller drops is the only requirement, then the drop can be broken by pushing it towards the exit of the slot, where the extensional rates rise due to the increase in the average velocity. However, a systematic study of the breakup process at constant strain rate is not possible with the current setup for high interfacial tension drops.

microfluidic channel leading up to the slot. The lower this resistance, the greater the maximum stress. Alternatively, one can employ pressure controllers with a higher pressure range. Also, the optimization of the geometry indicated in section 5.1.1 will yield higher values of k, producing higher strain rates.

5.1.4   Limitation on flow type

The analytical solution of the flow field is obtained with the assumption that the aspect ratio of the device, i.e., ratio of the microfluidic slot side length to the depth of the device, is high, around 10. At this high aspect ratio the flow in the microfluidic slot is Hele-Shaw flow which has no rotational characteristics. Thus, the flow type which can be generated in the current device is purely extensional. This limits the applicability of the device to be used in extensional rheology.

In order to obtain a rotational flow characteristic to the flow field the aspect ratio of the device should be less than 2 [17]. Moreover, even at this low aspect ratio the magnitude of the velocity near the device center in a purely rotational flow is very small as compared to the purely extensional flow. Thus, one has to come up with a new and improved design in order to have significant rotational flow at the device center.

5.1.5   Compatibility with material of construction of the microfluidic channel

The choice of the material of construction of the microfluidic channel is a crucial component of a successful experiment with the extensional flow device. Our experiments have been performed using PDMS-based microfluidic channels, because these are inexpensive and easy to fabricate. Unfortunately, PDMS presents compatibility issues when it is used with several liquids [36]. For example, while designing the experiments for chapter 4, the liquid combinations most commonly used to generate ultralow interfacial tensions (e.g. octane-water, heptane-water, decane-water, and hexadecane-water) were impossible to study in our device, because of the tendency of the organic phase to swell the microfluidic channel. Another problem posed by PDMS microchannels is that they tend to be fabricated with a bowing or sagging when the aspect ratio of the cross-section is large. This prevented us from building channels with aspect ratios greater than 10. Perhaps the severest difficulty of these channels is that if the surface is not treated correctly, soft particles tend to adhere to the channel walls, and cannot be moved by the flow.

This effect is accentuated when liquid combinations with high interfacial tensions are employed, which is another reason why such combinations were not studied with the device.

But now that we have standardized the design and operation of the device, we are ready to transition to a more stable platform – glass. Although glass-based microfluidic channels are more expensive, they are compatible with a much wider range of materials. They can be subjected to a variety of treatments to render them hydrophilic or hydrophobic. Unlike PDMS channels, they do not show bowing or sagging even for high aspect ratios. In the future, experiments will be performed with glass microfluidic channels.

5.2   Future work

5.2.1   Using the time scale of deformation to measure mechanical properties

For ultralow interfacial tension drops, the interfacial tension can be measured by a second method using our device. It was shown that when an extensional flow is imposed on a confined drop, it asymptotically reaches its steady shape over a time scale, t_c, given by Eq. 4.29. This means that if the shape of the drop is tracked with time, the interfacial tension can be deduced by fitting the time-dependent shape in Eq. 4.32. However, a precalculation of this time scale using a guess of the interfacial tension is advised. For high interfacial tensions, and low viscosity fluids, this time can be of the order of tens of microseconds. This technique is ideal for ultralow interfacial tensions and viscous suspending fluids.

5.2.2   Collision of soft particles to measure coalescence or adhesion rates

The extensional flow device can be used to implement controlled collisions between soft particles at defined strain rates. We have been able to perform a head-on collision between two drops, as may be seen in Fig. 2. The drops were created at a T-junction upstream of one of the channels leading up to the slot. The head-on collision was created by directing two drops using the control code into opposite ports in the slot, and then re-introducing them into the slot by reversing the flow.
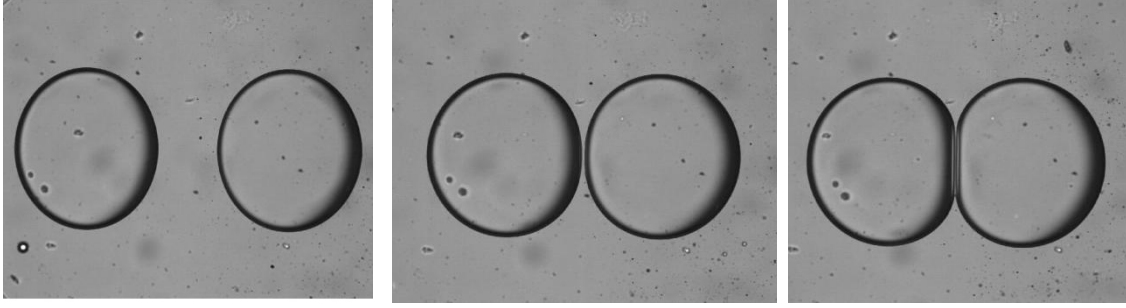
Figure 5.2 Image sequence showing head on collision of water droplet in highly viscous PDMS solution (5000 cp).

We also believe that our device can be used to collide two soft particles at predefined offsets. The strategy is as follows. The two drops are first confined in opposite exit channels, as shown in Fig. 5.3(a), close to the mouth of the entrance into the slot. The stagnation point is then moved to the position X_A with flow as shown in Fig.5. 3(b), in order to slow down the entrance of particle 1, and accelerate the entrance of particle 2. The flow is continued until particle 2 enters the slot and is displaced downwards by a predefined distance, δ_y; by this time, particle 1 also enters the slot [see Fig. 5.3(c)]. The stagnation point is then moved to center of mass of the two drops, $X_B\left(-\delta_x,-\delta_y/2\right)$, and flow is applied continuously until the droplets collide [see Fig. 5.3(d)]. The offset at the point of collision, Δ, can be tuned by adjusting δ, which, in turn, can be adjusted by changing X_A.

(a)   (b)
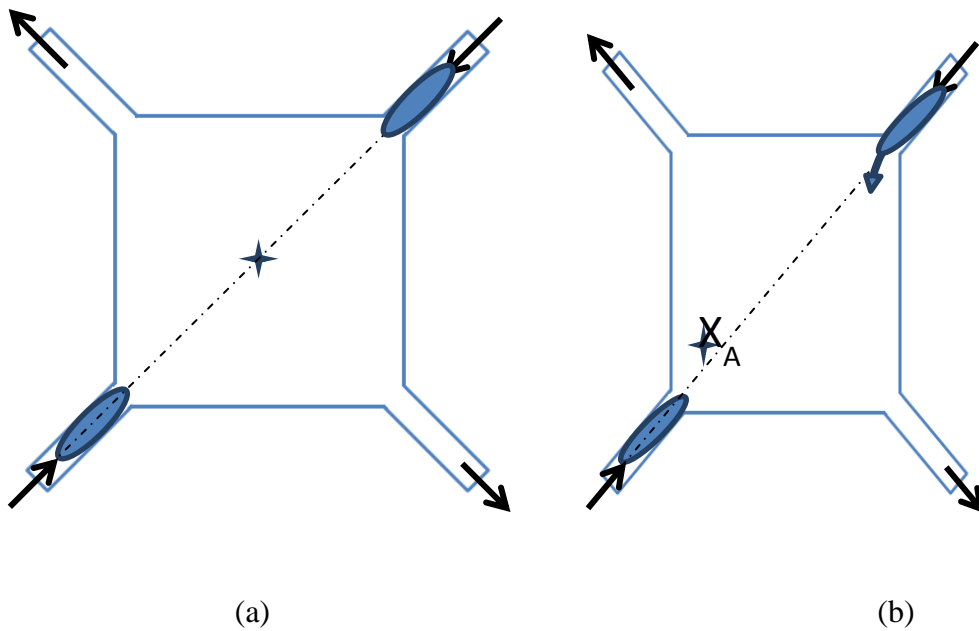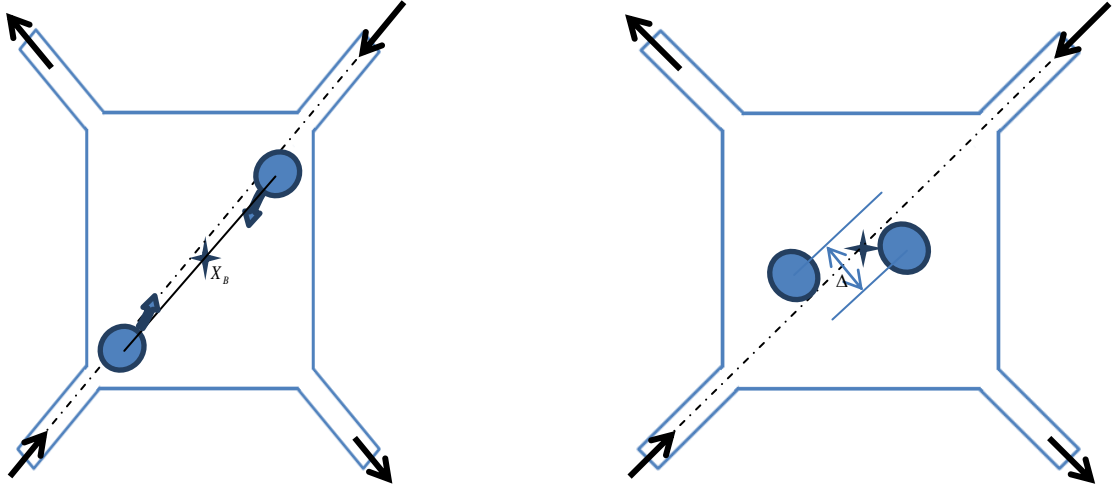
Figure 5.3. Strategy for producing offset between drops.

5.2.3   Stretching and collision of vesicles under confined conditions

Vesicles are soft particles in which a finite volume of liquid is enclosed by a membrane called the bilayer [37]. Although the dynamics of vesicles in different linear, unbounded flows have been studied extensively [38], there have been no studies for vesicles in linear flows under confined conditions. Our device can be easily used to study the stretching and breakup of vesicles. In a confined extensional flow, the capillary number for vesicle deformation is given by

$$Ca = \frac{\mu G \rho^5}{b^2 k_c},$$
(4.46)

where k_c is the bending modulus. Typical giant vesicles can be made up to 20 or 30 microns in size using electroformation [38], which means that for studying vesicles under confined conditions, one needs channels thinner than 20 microns. If we choose a channel depth of $2b = 10$ microns, for $k_c = 10^{-19}$ J and a confined initial radius of $\rho = 15$ microns, one can reach a capillary number of about 1 with stresses, μG, of only 10 μPa, which should be readily achievable with our device by adjusting the slot width, channel resistance and/or tube resistances [c.o. Eq. (4.44)].

5.2.4   Measuring bulk rheological properties in the device

A side capability of this device is that it also represents a platform for the investigation of the rheology of non-Newtonian fluids such as viscoelastic fluids, Bingham fluids, or shear thickening fluids. For this study, we do not need a drop of one fluid in another fluid, hence a device with four ports will suffice. The polymeric fluid is introduced through two inlets, generating a stagnation point flow at the center of the device. The rate of change of the polymeric fluid viscosity with the strain rate can then be calculated by determining the flow field as the strain rate in the central region of the device is changed by changing the pressure difference between the inlets and the outlets of the device.

In order to determine the flow field, the polymeric fluid could be seeded with fluorescent beads or other tracer particles, and μPIV study could be conducted to determine the position of the tracer particle with time. It should be noted that no particle trapping is required to deduce the power law of the polymeric fluid, and hence no active control of the flow field is required.

5.3   Summary

In this thesis, we have presented the construction and calibration of a microfluidic, extensional flow device for studying soft particles. We have also validated the device by demonstrating favorable agreement between interfacial tension measurements of an oil-water emulsion system with the device, and with a spinning drop tensiometer. The platform we have created will provide the ability to launch studies of deformation, breakup and coalescence/aggregation of a wide variety of soft-particle systems.

6   Bibliography

[1] T. Krebs, C. Schroën and R. Boom, "Coalescence kinetics of oil-in-water emulsions studied with microfluidics," *Fuel ,* vol. 106 , p. 327–334, 2013 .

[2] T. Krebs, K. Schroenb and R. Boom, "A microfluidic method to study demulsification kinetics," *Lab Chip ,* vol. 12 , p. 1060, 2012 .

[3] J. Sjöblom, Emulsions and Emulsion Stability, New York: Dekker, 1996.

[4] Y. S. Lipatov, V. F. Shumsky, I. P. Getmanchuk and A. N. Gorbatenko, "Rheology of polymer blends," *Rheol. Acta ,* vol. 21 , pp. 270-279 , 1982.

[5] M. J. Rosen, H. Wang, P. Shen and Y. Zhu, "Ultralow Interfacial Tension for Enhanced Oil Recovery at Very Low Surfactant Concentrations," *Langmuir ,* vol. 21 , pp. 3749-3756 , 2005 .

[6] W. M. Saltzman, "Cost-Reducing Protein Production and Delivery for Sexually Transmitted Disease Prevention," *IEEE Eng. Med. Biol. Mag.,* vol. 22 , p. 43–50 , 2003.

[7] C. Gosse and V. Croquette, "Magnetic Tweezers: Micromanipulation and Force Measurement at the Molecular Level," *Biophys. J.,* vol. 82, p. 3314–3329, 2002.

[8] H. Lee, A. M. Purdon and R. M. Westervelt, "Manipulation of biological cells using a microelectromagnet matrix," *Appl. Phys. Lett. ,* vol. 85 , p. 1063 , 2004.

[9] A. Ashkin, J. M. Dziedzic, J. E. Bjorkholm and S. Chu, "Observation of a single-beam gradient force optical trap for dielectric particles," *Opt. Lett.,* vol. 11, p. 288–290, 1986.

[10] A. Ashkin, "History of Optical Trapping and Manipulation of Small-Neutral Particle, Atoms, and Molecules," *IEEE J. Sel. Topics Quantum Electron.,* vol. 6, no. 6, pp. 841-856, 2000.

[11] B. B. P. J. Woodside SM, "Measurement of ultrasonic forces for particle-liquid separations," *Aiche Journal,* vol. 43, pp. 1717-1736, 1997.

[12] J. Lee, S. Teh, A. Lee, H. Kim, C. Lee and K. Shung, "Transverse acoustic trapping using a Gaussian focused ultrasound," *Ultrasound Med Biol. ,* vol. 36, no. 2, pp. 350-355, 2010.

[13] W. Coakley, "Ultrasonic separations in analytical biotechnology.," *Trends Biotechnol.,* vol. 15, no. 12, pp. 506-511, 1997.

[14] G. I. Taylor, "The Formation of Emulsions in Definable Fields of Flow," *Proc. R. Soc. London,* vol. 146, p. 501–523, 1934.

[15] B. J. Bentley and G. L. Leal, "A computer-controlled four-roll mill for investigations of particle and drop dynamics in two-dimensional linear shear flows," *J. Fluid Mech.,* vol. 167, p. 219–240, 1986.

[16] C. M. Schroeder, H. P. Babcock, E. S. G. Shaqfeh and S. Chu, "Observation of Polymer Conformation Hysteresis in Extensional Flow," *Science ,* vol. 301, p. 1515 , 2003.

[17] J. S. Lee, R. Dylla-Spears, N. P. Teclemariam and S. J. Muller, "Microfluidic four-roll mill for all flow types," *Appl. Phys. Lett. ,* vol. 90 , 2007.

[18] M. D. Armani, S. V. Chaudhary, R. Probst and B. Shapiro, "Using Feedback Control of Microflows to Independently Steer Multiple Particles," *Microelectromech. Syst.,* vol. 15 , p. 945–956, 2006 .

[19] K. C. Neuman and S. M. Block, "Optical trapping," *Rev. Sci. Instrum.,* vol. 75 , p. 2787 , 2004.

[20] K. Svoboda and S. M. Block, "Biological Applications of Optical Forces," *Annu. Rev. Biophys. Biomol. Struct.,* vol. 23, p. 247, 1994.

[21] M. Tanyeri, M. Ranka, N. Sittipolkula and C. M. Schroeder, "A microfluidic-based hydrodynamic trap: design and implementation," *Lab Chip,* vol. 11, p. 1786, 2011 .

[22] M. Borrell, Y. Yoon and G. L. Leal, " Experimental analysis of the coalescence process via head-on collisions in a time-dependent flow," *Physics of Fluids,* vol. 16, no. 11, p. 3945−3954, 2004.

[23] Y. T. Hu, D. J. Pine and L. G. Leal, "Drop deformation, breakup, and coalescence with compatibilizer," *Phys. Fluids ,* vol. 12, p. 484 , 2000.

[24] S. D. Hudson, F. R. Phelan, M. D. Handler, J. T. Cabral and K. B. Migler, "Microfluidic analog of the four-roll mill," *Appl. Phys. Lett. ,* vol. 85, p. 335 , 2004.

[25] M. Armani, S. Chaudhary, R. Probst, S. Walker and B. Shapiron, "Control of microfluidic systems: Two examples, results, and challenges," *Int. J. Robust. Nonlin. Control ,* vol. 15 , no. 16, p. 785−803, 2005 .

[26] A. E. Cohen and W. E. Moerner, "Suppressing Brownian Motion of Individual Biomolecules in Solution," *Proc. Natl. Acad. Sci. U.S.A. ,* vol. 103 , no. 12, p. 4362−4365, 2006.

[27] A. E. Cohen and W. E. Moerner, "Controlling Brownian motion of single protein molecules and single fluorophores in aqueous buffer," *Opt. Express ,* vol. 16 , no. 10, p. 6941−6956, 2008 .

[28] A. P. Fieldsa and A. E. Cohen, *Proc. Natl. Acad. Sci. U.S.A. ,* vol. 108 , no. 22, p. 8937−8942, 2011 .

[29] M. Tanyeri and C. M. Schroeder, "Manipulation and Confinement of Single Particles Using Fluid Flow," *Nano Lett.,* vol. 13 , no. 6, p. 2357–2364, 2013.

[30] J. L. Cayias, R. S. Schechter and W. H. Wade, "The Measurement of Low Interfacial Tension via the Spinning Drop Technique," in *Adsorption at Interfaces*, Washington , American Chemical Society, 1975, pp. 234-247.

[31] S. S. H. Tsai, J. S. Wexler, J. Wan and H. A. Stone, "Microfluidic ultralow interfacial

tensiometry with magnetic particles," *Lab Chip,* vol. 13 , p. 119, 2013 .

[32] J. C. McDonald and G. M. Whitesides, "Poly(dimethylsiloxane) as a Material for Fabricating Microfluidic Devices," *Acc. Chem. Res. ,* vol. 35 , no. 7, p. 491–499, 2002 .

[33] P. Garstecki, M. J. Fuerstman, H. A. Stone and G. M. Whitesides, "Formation of droplets and bubbles in a microfluidic T-junction—scaling and mechanism of break-up," *Lab Chip,* vol. 6, p. 437–446, 2006.

[34] B. Vonnegut, "Rotating Bubble Method for the Determination of Surface and Interfacial Tensions," *Rev. Sci. Instrum.,* vol. 13, no. 6, p. 6–9, 1942.

[35] S. J. Haward, M. S. N. Oliveira, M. A. Alves and G. H. McKinley, "Optimized Cross-Slot Flow Geometry for Microfluidic Extensional Rheometry," *Phys. Rev. Lett.,* vol. 109, p. 128301, 2012.

[36] J. N. Lee, C. Park and G. M. Whitesides, "Solvent Compatibility of Poly(dimethylsiloxane)-Based Microfluidic Devices," *Anal. Chem. ,* vol. 75, pp. 6544-6554, 2003.

[37] J. N. Israelachvili, Intermolecular and surface forces, Amsterdam, MA : Academic Press, 2011.

[38] P. L. Luisi and P. Walde, Giant vesicles, Chichester: Wiley, 2000..

[39] H. Hu and D. Joseph, "Evolution of a Liquid Drop in a spinning Drop Tensiometer," *Colloid Interface Sci.,* vol. 162, no. 2, pp. 331-339, 1994.

Appendix A
Analytical solution for extensional flow in the diamond

The schematic of the diamond is shown in the figure A.1. The inlet and outlets are assumed to be point inlets and outlets. Since the flow between two parallel plates separated by infinitely small gap is a Hele-Shaw flow, thus the governing equation and the boundary condition are as follows.

$$\frac{\partial^2 \psi}{\partial x^2} + \frac{\partial^2 \psi}{\partial y^2} = 0,$$

$$\psi\big|_{y=0} = 0, \qquad \psi\big|_{y=1} = \psi_2, \tag{.47}$$

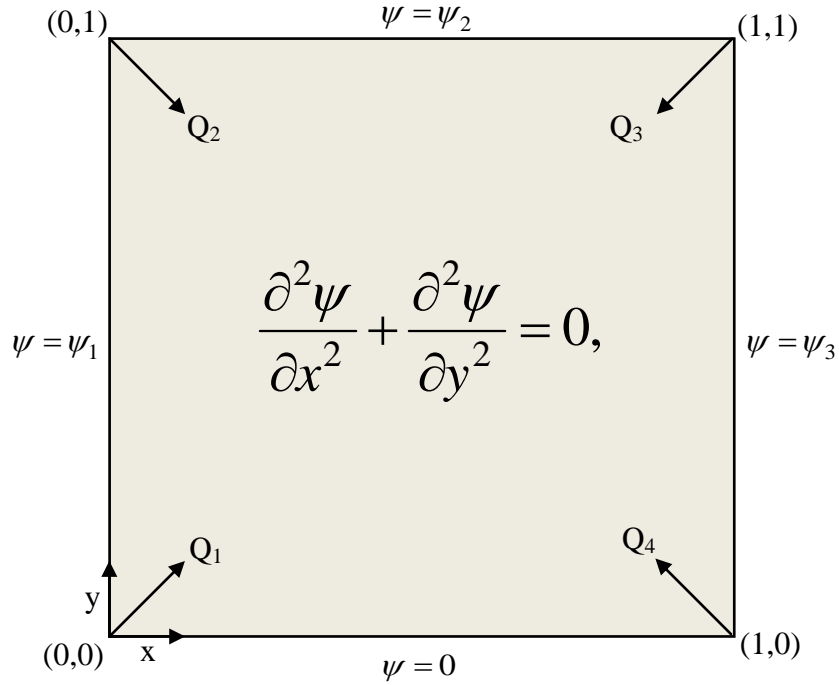$$\psi\big|_{x=0} = \psi_1, \qquad \psi\big|_{x=1} = \psi_3,$$

Figure A.1 Governing equation and boundary conditions.

The general solution of the Laplace equation is of following form

$$\psi = y\psi_2 + \sum_{n=1}^{\infty}\left\{A_n \sinh\left[n\pi(1-x)\right] + B_n \sinh(n\pi x)\right\}\frac{\sin(n\pi y)}{\sin(n\pi y)} \qquad (.48)$$

Equation (.48) satisfies the governing equation and the boundary conditions in y.

The boundary condition at $x = 0$ is,

$$\psi_1 = y\psi_2 + \sum_{n=1}^{\infty} A_n \sin(n\pi y) \qquad (.49)$$

To satisfy the boundary conditions in Eq. (.49), we use biorthogonality,

$$\begin{aligned}
A_n &= 2\int_0^1 (\psi_1 - y\psi_2)\sin(n\pi y)\,dy \\
&= 2\left[\frac{\psi_1}{n\pi}\left[1 - \cos(n\pi)\right] - \psi_2\left[-\frac{1}{n\pi}y\cos(n\pi y) + \frac{1}{n^2\pi^2}\sin(n\pi y)\right]\Big|_0^1\right] \\
&= \frac{2}{n\pi}\left\{\psi_1\left[1 - \cos(n\pi)\right] + \psi_2\cos(n\pi)\right\} \\
&= \frac{2}{n\pi}\left\{\psi_1 + (\psi_2 - \psi_1)\cos(n\pi)\right\}
\end{aligned} \qquad (.50)$$

Similarly, using the boundary conditions at $x = 1$, we get

$$B_n = \frac{2}{n\pi}\left\{\psi_3 + (\psi_2 - \psi_3)\cos(n\pi)\right\} \qquad (.51)$$

Hence, the solution to Eq. (.47) is,

$$\psi = y\psi_2 + \sum_{n=1}^{\infty}\frac{2}{n\pi}\left\{\begin{array}{l}\left[\psi_1 + (\psi_2 - \psi_1)\cos(n\pi)\right]\sinh\left[n\pi(1-x)\right] \\ +\left[\psi_3 + (\psi_2 - \psi_3)\cos(n\pi)\right]\sinh(n\pi x)\end{array}\right\}\frac{\sin(n\pi y)}{\sinh(n\pi)} \qquad (.52)$$

The relationship between ψ_i and the inlet and outlet flow rates are

$$\psi_1 = Q_1$$
$$\psi_2 = Q_1 + Q_2 \qquad (.53)$$
$$\psi_3 = Q_1 + Q_2 + Q_3$$

Form conservation of mass the flow rate $Q_4 = -\left(Q_1 + Q_2 + Q_3\right)$. The velocity field is obtained as follows,

$$u = \frac{\partial \psi}{\partial y} = \psi_2 + \sum_{n=1}^{\infty} 2 \left\{ \begin{array}{l} \left[\psi_1 + (\psi_2 - \psi_1)\cos(n\pi)\right]\sinh\left[n\pi(1-x)\right] \\ + \left[\psi_3 + (\psi_2 - \psi_3)\cos(n\pi)\right]\sinh(n\pi x) \end{array} \right\} \frac{\cos(n\pi y)}{\sinh(n\pi)}$$

$$v = -\frac{\partial \psi}{\partial x} = \sum_{n=1}^{\infty} 2 \left\{ \begin{array}{l} \left[\psi_1 + (\psi_2 - \psi_1)\cos(n\pi)\right]\cosh\left[n\pi(1-x)\right] \\ - \left[\psi_3 + (\psi_2 - \psi_3)\cos(n\pi)\right]\cosh(n\pi x) \end{array} \right\} \frac{\sin(n\pi y)}{\sinh(n\pi)}$$

$$(.54)$$

At the stagnation point $\left(x_s, y_s\right)$,

$$u\left(x_s, y_s\right) = v\left(x_s, y_s\right) = 0. \qquad (.55)$$

Thus the position of the stagnation point is a function of ψ_i and thus a function of Q_i.

Appendix B

Device Center and Edge Determination

The equation of the edges forming the diamond are obtained from the points, c_i on each arm (see fig 3.1) .

$$L_i : -M_i x + y = C_i \tag{B.1}$$

Here, M_i and C_i are the slope and intercept of the line L_i respectively.

The intersections of the edges are calculated by the solving the following system of linear equation.

$$\begin{bmatrix} -M_i & 1 \\ -M_j & 1 \end{bmatrix} \begin{bmatrix} x \\ y \end{bmatrix} = \begin{bmatrix} C_i \\ C_j \end{bmatrix} \tag{B.2}$$

Solving equation (B.2) we get the co-ordinates of the device corners. The equation of the diagonals is then obtained from the corner points.

Then the device center is obtained by calculating the intersection of the diagonals formed. The length of the edge of the diamond is calculated by the following equation,

$$L_e = (d_1 + d_2)/2\sqrt{2} \tag{B.3}$$

Where L_e is the edge length of the device and d_1, d_2 are the length of the diagonals.

Appendix C
GUI Description

A Matlab Graphical User Interface (GUI) is created to facilitate the trapping of a particle/drop. Fig. C.1 shows the user interface used to trap the particle. The left half of the user interface is used to define the pressure of the inlets and the outlets. When the program is running in manual mode, the 'Manual Control' consol is active and the pressure of all the reservoirs can be varied independently. This is used to bring the particle near the center of the device by changing the pressure of either of the inlet or outlets.
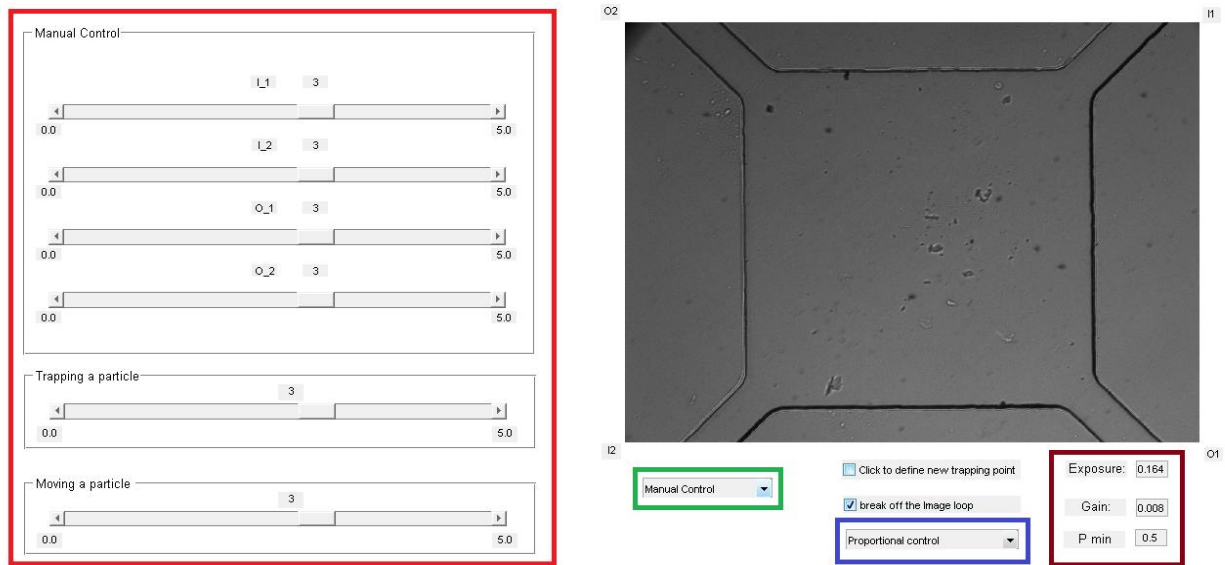

Figure C.1 The GUI interface used to trap and manipulate a particle. Consol highlighted by red box is used to change the reservoir pressure. Drop down menu highlighted by green box is used to toggle between 'manual control', 'Particle trapping' and 'Particle steering'. Drop down menu highlighted by blue box is used to toggle between 'Proportional control' and 'Model predictive control'. Consol highlighted by brown box can used to change exposure time, proportional gain and the outlet pressure for particle trapping and steering.

Once the particle is near the device center then Particle trapping is selected from the drop down menu (green box). Trapping a particle consol becomes active and the user then can change the inlet pressure. Outlet pressure can be changed by changing the value of 'P_min' (brown box). Thus the user can change the strain rate applied by changing the difference in the inlet and outlet

pressures. The gain of the proportional control can be changed by changing the value of 'Gain' (brown box). Decreasing the gain decreases the rate at which particle approaches the device center and increasing the gain leads to oscillation near the stagnation point. Thus a proper gain should be chosen. After some trial and error we found that the gain of 0.008 was optimal. The user can also change the exposure time in order to view the particle more clearly by changing the value of 'Exposure' (brown box). The increase in exposure time makes the particle more bright and thus easy to view but on the other hand it increases the time taken for reading the image. We found that the exposure time of 0.164 sec was good for particle trapping and 0.0164 sec was optimal for drop trapping and stretching.

For steering a particle in a predefined path, a particle is first trapped at the device center and 'Particle steering' is chosen from the drop down menu (green box). Again, the inlet and outlet pressure and thus the strain rate can be changed to steer a particle at a desired rate.

Additionally, a code for particle trapping using a model predictive control is also written. So the user can choose either 'Proportional control' or 'MPC control' from the drop down menu (blue box). For the present experiments the proportional control was sufficient and thus only proportional control was used to trap and manipulate a particle/drop.